Applied Catalysis B: Environmental 341 (2024) 123330

Contents lists available at ScienceDirect

Applied Catalysis B: Environmental

journal homepage: www.elsevier.com/locate/apcatb

Insight into the synergistic effect of copper and sodium over metal organic framework-derived Fe-based catalyst for CO_2 hydrogenation to aromatics

Chonghao Chen, Guiyao Song, Zihao Wang, Jianhua Song, Qisheng Jiang, Yangzhou Zhai, Dianhua Liu *

Engineering Research Center of Large-Scale Reactor Engineering and Technology, Ministry of Education, State Key Laboratory of Chemical Engineering, School of Chemical Engineering, East China University of Science and Technology, Shanghai 200237, China

ARTICLE INFO

Keywords:
CO_2 hydrogenation
Aromatics
Fe-based catalyst
Na-Cu synergy

ABSTRACT

One-step hydrogenation of carbon dioxide (CO_2) to aromatics is a promising strategy for relieving the stress of fossil fuels. Here, a copper and sodium co-modified Fe-based catalyst (3-NFC-5) was synthesized through the pyrolysis of Cu-doped MIL-101(Fe) and Na impregnation. After combining with HZSM-5, 42.11% CO_2 conversion and 50.68% total aromatics selectivity was achieved. Through multiple characterization and DFT calculations, the synergistic promotion of Na and Cu on light olefins intermediate production was revealed. Na was crucial for COOH* formation as the intermediate for reverse water gas shift reaction (RWGS), whose concentration could be further enhanced after Cu modification. Controlled C-C coupling towards C_2-C_4 hydrocarbons was realized by the enhanced CO non-dissociative activation and the increased content of χ-Fe_5C_2 after Cu doping, which was responsible for the inhibited surface CH_x* concentration and selective production of light olefins, respectively.

1. Introduction

Comprehensive utilization of CO_2 has attracted widespread attention under the stimulation of carbon-neutral prospect [1]. Above all, converting CO_2 to various value-added products is a promising strategy that not only reduces CO_2 emission, but also alleviates the huge demand of ever-dwindling fossil resources [2]. Aromatics, especially benzene, toluene and xylene (BTX), are crucial platform chemicals in chemical industry to produce polymers, medicines and dyestuff [3], gathering steadily growing market demand world-widely. Thus, CO_2 direct hydrogenation to aromatics sheds lights on a novel pathway for non-fossil fuel production, appealing notable attraction in CO_2 utilization [4].

Aromatics production via CO_2 hydrogenation has been successfully implemented on multifunctional metal oxide-zeolite catalysts [5,6], and the research mainly focused on Methanol-mediated route and modified Fischer-Tropsch synthesis (FTS) route, which are summarized in Table S1. For the modified-FTS route, Fe-based catalysts were commonly utilized [7,8], as these catalysts had intrigued greatest attention because of its high selectivity towards olefins [9,10]. In this case, light olefins, which were acknowledged as important intermediates in the tandem reaction [11,12], are firstly formed over Fe-based catalysts through consecutive RWGS and FTS, followed by oligomerization, cyclization and dehydrogenation or hydrogen transformation to form aromatics over acid sites of HZSM-5 [13,14]. Besides, aliphatic hydrocarbons with five or more carbon atoms generated via successive C-C coupling over Fe-based catalysts may crack into C_1-C_4 paraffins with weak aromatization ability on acid sites of HZSM-5, reducing carbon atomic efficiency for light olefins production [15]. Thus, promoting the selective transformation of reactants into light olefins and inhibiting C-C chain growth possesses great significance in elevating aromatics selectivity.

Fe_3O_4 was broadly considered as the active phase for RWGS, while surface oxygen vacancies (O_v) were vital for CO_2 adsorption and activation [16,17]. Gu et al. [18] discovered that proper loading of Fe on ZrO_2-supported catalyst could optimize the concentration of O_v, thus increasing CO_2 conversion. Another research by our group [17] revealed that CO reduction created more surface O_v on bulk Fe-based catalysts, achieving fabulous CO_2 conversion and restrained CO selectivity. However, the adsorption and activation state of CO_2 on O_v-participating Fe-based surface was still unclear. Besides, Na was a widely-used dopant for enhancing CO_2 adsorption and C-C coupling because of its basic property [19]. Nevertheless, the potential risk of excessive C-C coupling by sole Na modification which generated high C_{5+} and constrained light olefins selectivity deserved further improvement for selective production of short chain olefins [20]. In order to weaken the chain-growth

* Corresponding author.
E-mail address: dhliu@ecust.edu.cn (D. Liu).

https://doi.org/10.1016/j.apcatb.2023.123330
Received 5 July 2023; Received in revised form 20 September 2023; Accepted 22 September 2023
Available online 24 September 2023
0926-3373/© 2023 Elsevier B.V. All rights reserved.

reaction, Liang et al. [21] used Mn-decorated NaFe catalysts and obtained enriched Fe_5C_2 phase, while inhibited CO adsorption could explain the restrained chain growth reaction, but CO_2 conversion of 38.6% needed in-depth improvement. Recently, a study by our group which focused on Na-Cu synergy effect among Fe-Cu-Na ternary metal oxide confirmed the catalytic promotion caused by bi-metal doping, accelerating the dissociation and uptake of intermediates and achieving high aromatics selectivity [22]. However, convincing clarification of the mechanism how Cu and Na accelerate the activation and dissociation of reactants and intermediates is still of great urgency.

Metal organic frameworks (MOF) with ordered morphology and tunable structure have attracted significant research attention in heterogeneous catalysis [23]. Apart from the firsthand use of MOF as solid catalysts, applying MOF as a sacrifice template to generate diverse active nanoparticles is also a promising route [24]. Compared with traditional catalysts, MOFs-derived catalysts provided highly dispersed nano particles due to their unique structure and textual properties [25], and presented improved physicochemical properties, enhanced metal-support interactions as well as better catalytic performance [26]. For aromatics synthesis, wang et al. [27] prepared Na-Fe@C/HZSM-5 catalyst by pyrolysis of iron-based MOFs under N_2 atmosphere, in which the carbon layer derived from ligands decomposition successfully inhibit the aggregation and deactivation of iron species, utilizing the exposed active sites in a substantial degree. Except from the studies that focus on unitary-metal MOFs as heat precursors, post modification methods of MOFs before heat treatment to introduce diverse hetero-atoms into MOF structure are rarely reported in CO_2 hydrogenation to aromatics. Thus, properties of these poly-metallic catalysts derived from post-modified MOFs deserve profound research.

Herein, a Cu and Na co-modified Fe based catalyst was synthesized by direct pyrolysis of Cu-doped MIL-101(Fe) under air atmosphere. After mixing with HZSM-5, the multifunctional catalyst exhibited 42.11% of CO_2 conversion and 50.68% of total aromatics selectivity, with undesirable CH_4 selectivity suppressed at 8%. With multiple characterizations and DFT calculations, the synergy effect between Cu and Na on preferential production of light olefins and inhibition of C_{5+} over Fe-based catalysts was clarified. Na was crucial for COOH* formation as the intermediate for reverse water gas shift reaction (RWGS), whose concentration could be further enhanced after Cu modification. Controlled C-C coupling towards C_2-C_4 hydrocarbons was realized by the enhanced CO non-dissociative activation and the increased content of χ-Fe_5C_2 after Cu doping, which was responsible for the inhibited surface CH_x* concentration and selective production of light olefins, respectively.

2. Experimental section

2.1. Catalysts preparation

2.1.1. Preparation of MIL-101(Fe)

MIL-101(Fe) was synthesized according to a previous paper [1]. Typically, 4.669 g terephthalic acid (H_2BDC) and 15.046 g ferric trichloride hexahydrate ($FeCl_3{\cdot}6H_2O$) were dissolved in 350 ml *N, N*-dimethylformamide (DMF) and continuously stirred for 30 min until the mixture became homogeneous. The calculated molar ratio of $FeCl_3{\cdot}6H_2O$ against H_2BDC was 2:1. Afterwards, the solution was transferred into Teflon-lined auto claves and heated at 110 ℃ for 20 h. After cooling to room temperature, the product was obtained via centrifugation, washed with DMF and ethanol for three times and dried at 70 ℃ overnight. All samples were activated at 150 ℃ for 4 h before further use.

2.1.2. Preparation of xCu@MOF and y-NFC-x catalysts

xCu@MOF (x represents the Cu molar ratio in the precursor) was prepared by double-metal MOF method [2]. Typically, a total metal (Cu+Fe): ligand molar ratio was fixed as 2:1, and Cu was introduced into the precursor solution by partially replacing $FeCl_3{\cdot}6H_2O$ with cupric chloride ($CuCl_2$) with Cu molar ratios of 2.5%, 5%, 10%, and 18%. The subsequent hydrothermal and purification process was as same as MIL-101 synthesis. The as-synthesized xCu@MOF catalysts were calcined at 400 ℃ with a heating rate of 2 ℃/min in a muffle furnace under static air atmosphere for 4 h. y-NFC-x catalysts were prepared by Na doping through incipient wetness impregnation method using Na_2CO_3 as Na source on the calcined catalysts, where y represented the calculated Na weight ratio.

Commercial HZSM-5 was purchased from Nankai University.

2.2. Catalysts test

CO_2 hydrogenation was carried out in a 316 L stainless fixed-bed reactor with a tube diameter of 10 mm. Before the reaction, all the catalysts were crushed and sieved into granules of 40–60 mesh. Typically, for aromatics synthesis, 1 g bifunctional catalyst (0.5 g y-NFC-x + 0.5 g HZSM-5) obtained by granule mixing was used unless otherwise stated. For CO_2-FTS synthesis, 1 g y-NFC-x catalyst was used. The catalyst was firstly in-situ reduced in a 60% H_2/N_2 flow (100 ml/min) at 350 ℃ for 12 h at ambient pressure. After cooling the reactor to 320 ℃, the reaction gas ($CO_2/H_2/N_2$ =24/72/4) with a total flow rate of 25 ml/min was pumped into the reactor and the system was pressured to 3 MPa. The heavy products were separated by condensation and analyzed by PerkinElmer Clarus 580 gas chromatograph. The gaseous products were detected on an online gas chromatograph (7890B, Agilent) equipped with a thermal conductor detector (TCD) for H_2, N_2, CO and CO_2 analysis and a flame ionization detector (FID) for the separation and detection of light hydrocarbons.

Catalysts characterization, calculation methods and DFT calculation details could be found in the Supporting Information.

3. Results and discussion

3.1. Characterization of the xCu@MOF precursors

It could be seen from Fig. S1a that the pristine MIL-101(Fe) precursor displayed identical octahedral morphology, while XRD patterns (Fig. S2) of MIL-101(Fe) displayed characteristic peaks at 9.0, 9.4, 9.6 and 18.8°, indicating the successful synthesis of MIL-101(Fe) [28]. With the increase of Cu content, the as-prepared xCu@MOF presented more irregular morphology with rough surface and declining particle size (Fig. S1b-d), suggesting that Cu embedding into MIL-101 framework was deleterious to the original regular morphology. Moreover, along with the increase of Cu content in precursor, the intensity of the characteristic peaks of MIL-101(Fe) gradually decreased (Fig. S2), indicating that the adulteration of Cu atoms into MIL-101 structure favored the formation of less crystallized MOF. For the 18Cu@MOF catalyst (Fig. S1d), especially, sheet-like structure was first witnessed, which could be attributed to the formation of Cu-BDC [29]. This could be ascribed to the regional elemental enrichment at high Cu concentration, which was evidenced by the new peak appeared at about 10.7° (Fig. S2) belonging to the (220) lattice plane of Cu-BDC [30]. Furthermore, FT-IR spectra (Fig. S3) of 5Cu@MOF further confirmed successful formation of MOF structure. Comprehensively, peaks at 1687, 1597 and 1392 cm^{-1} represented C═O stretching vibration, symmetric and asymmetric stretching of OCO functional group in H_2BDC ligands, while two peaks located at 1508 and 753 cm^{-1} could be attributed to C═C stretching and C-H bending stretching vibration related to benzene rings [31,32]. Except for the peak at 553 cm^{-1} related to the metal-oxide bond Fe-O [33], the peak at 1026 cm^{-1} was associated with C-O-Cu stretching in the MOF structure, indicating the successful doping of Cu into the framework [34].

3.2. Structure, morphology and electron properties of fresh 3-NFC-x catalysts

The 3-NFC-x catalysts were obtained from MIL-101(Fe) and the xCu@MOF via calcination at 400 ℃ and subsequent Na impregnation using Na_2CO_3 as Na source. The calcination process of MIL-101(Fe) and 5Cu@MOF was studied by TGA (Fig. S4). The first stage between RT to 100 ℃ showed a weight loss of ~3%, which could be attributed to removal of adsorbed H_2O [35]. The second stage (about 100–300 ℃) was owing to the loss of free terephthalates in the pores while the collapse of MOF framework and oxidation of ligands H_2BDC accounted for the third stage (about 300–400 ℃) [36]. In detail, the collapse of MOF initiated at 283 ℃ and ended at 376 ℃ for 5Cu@MOF, which were both lower than that of MIL-101(Fe) (295 ℃ and 431 ℃), indicating that Cu addition weakened the thermal stability of MOF framework.

Table S2 showed ICP-OES results of actual Na and Cu contents of y-NFC-x catalysts. An upper limit of 2.07 wt% Cu was observed for 3-NFC-18 catalyst, implying that the extraction of Cu into the MOF lattice was constrained. Besides, the actual Na content was approximate to the calculated data.

As is shown in SEM photographs (Fig. S5), the 3-NFC-x catalysts presents irregular morphology with tiny nanoparticles evenly covered over the catalyst surface. Moreover, it could be observed that the 3-NFC-x catalysts hardly retained the initial octahedral morphology of MIL-101, suggesting that calcination under air atmosphere at 400 ℃ generated almost complete degradation of MOF frameworks. Additionally, the particle size of 3-NFC-x catalysts calculated by Scherrer equation (Table S3) showed a declining trend with the increase of Cu content, suggesting that Cu addition favored formation of smaller particles. Fig. 1a illustrated the XRD patterns of the 3-NFC-x catalysts with different Cu concentration, where the major crystalline phase was found to be Fe_2O_3 while no peak belonging to Cu or Na based species was detected in all 3-NFC-x catalysts, suggesting the uniform dispersion and the relatively low content of Cu and Na compared with Fe, highly consistent with HAADF-STEM and element mapping of 3-NFC-5 catalyst (Fig. 2). In addition, Fig. 1b displayed the magnified XRD between 32° and 37°. The peaks slightly shifted to lower 2 Theta degree along with the increase of Cu content, indicating the inset of Cu into the Fe_2O_3 lattice [37]. TEM images (Fig. 2d, h) further exhibited that particles with larger size tended to stack compactly, with particles of smaller size adhering to the surface, creating abundant intergranular mesopores. HRTEM (Fig. 2d) of 3-NFC-5 catalyst confirmed that Fe_2O_3 was the main crystalline phase in 3-NFC-5 catalyst. The characteristic crystal spacings of 0.24 nm for Fe_2O_3 (110) and 0.36 nm for Fe_2O_3 (012) lattice plane were observed, fitting well with the XRD results.

Fig. S6a listed the N_2 physical adsorption-desorption isotherms of 3-NFC-x catalysts. The isotherms show typical type IV curves with H3 type hysteresis loop, indicating the irregular pore structure and existence of mesopores [38]. With the increase of Cu content, the BET surface area of 3-NFC-x catalysts was raised from about 16 m^2/g to 19 m^2/g, 23 m^2/g, 28 m^2/g, respectively, which was consistent with the decreased particle size. The increased pore volume and pore size (Fig. S6b and Table S3) after Cu modification suggested that Cu addition could probably inhibit the aggregation of small crystals, providing more exposed active sites for CO_2 hydrogenation.

XPS results in the Fe 2p region of y-NFC-x catalysts (Fig. 3a, b and Table S4) revealed the surface electronic properties after modification by Na and Cu. As shown, the high-resolution peaks at about 725 eV and 710 eV represented Fe $2p^{1/2}$ and Fe $2p^{3/2}$, respectively. For Fe $2p^{3/2}$ region, the peaks were further divided into Fe^{3+} and Fe^{2+} [39]. With the increase of Na content from 0% to 3%, the doublet of Fe^{3+} in Fe 2p shifted ~0.6 eV to a lower binding energy. However, further increase of Na content to 12% only contributed for a 0.26 eV decrease. Thus, it could be speculated that a moderate Na amount facilitated electron transfer from Na to Fe, leading to increased surface basicity. Nevertheless, superfluous Na had little effect on electron transfer. For the 3-NFC-x with different Cu contents, similar phenomena could be observed despite smaller binding energy shift compared with y-NFC-5 (0.29 eV decrease from 3-NFC-0–3-NFC-5), indicating the weaker electron transfer of Cu than Na. For O 1 s spectra (Fig. 3c, d), binding energies at 529 eV, 531 eV and 533 eV could be ascribed to lattice oxygen, adsorbed oxygen on defects and surface adsorbed OH/H_2O [40]. It could be concluded that moderate Cu decoration on 3-NFC-5 generated most O_v (37.44%), but further addition of Cu decreased the O_v ratio, indicating the best CO_2 adsorption performance for 3-NFC-5. Besides, Na decoration could linearly increase the O_v concentration to 40.4% on 12-NFC-5, suggesting Na could promote the formation of surface O_v. This could be explained by increased surface Fe^{2+}/Fe^{3+} ratio along with the addition of Na content (Table S4), as Na accelerated the formation of Fe^{2+} in octahedrally coordinated sites, which favored formation of surface O_v [41]. Na 1 s XPS spectra (Fig. S7a and Table S5) indicated the highest binding energy of Na in 3-NFC-5 among 3-NFC-x, suggesting the electron donation from Na to Fe was most significant on 3-NFC-5, while increase of Na from 5% to 12% only observed a tiny lift of 0.34 eV, matching well with the Fe 2p XPS. Besides, electron transfer from Na to Cu was not observed as the binding energy of Cu shifted to higher value

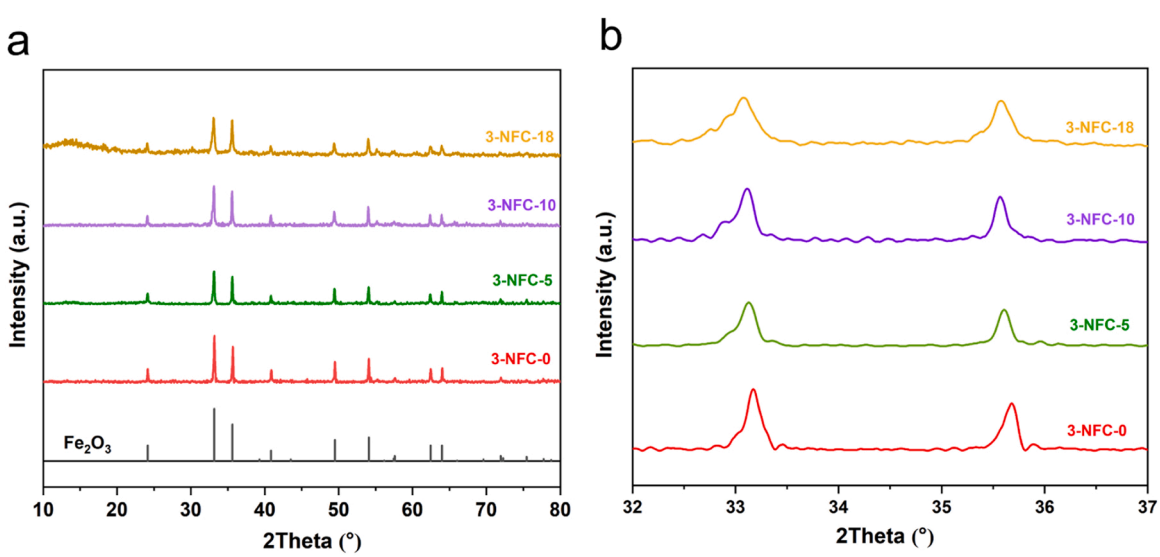

Fig. 1. XRD patterns (a) and magnified detail XRD between 32° and 37° (b) of 3-NFC-x catalysts.

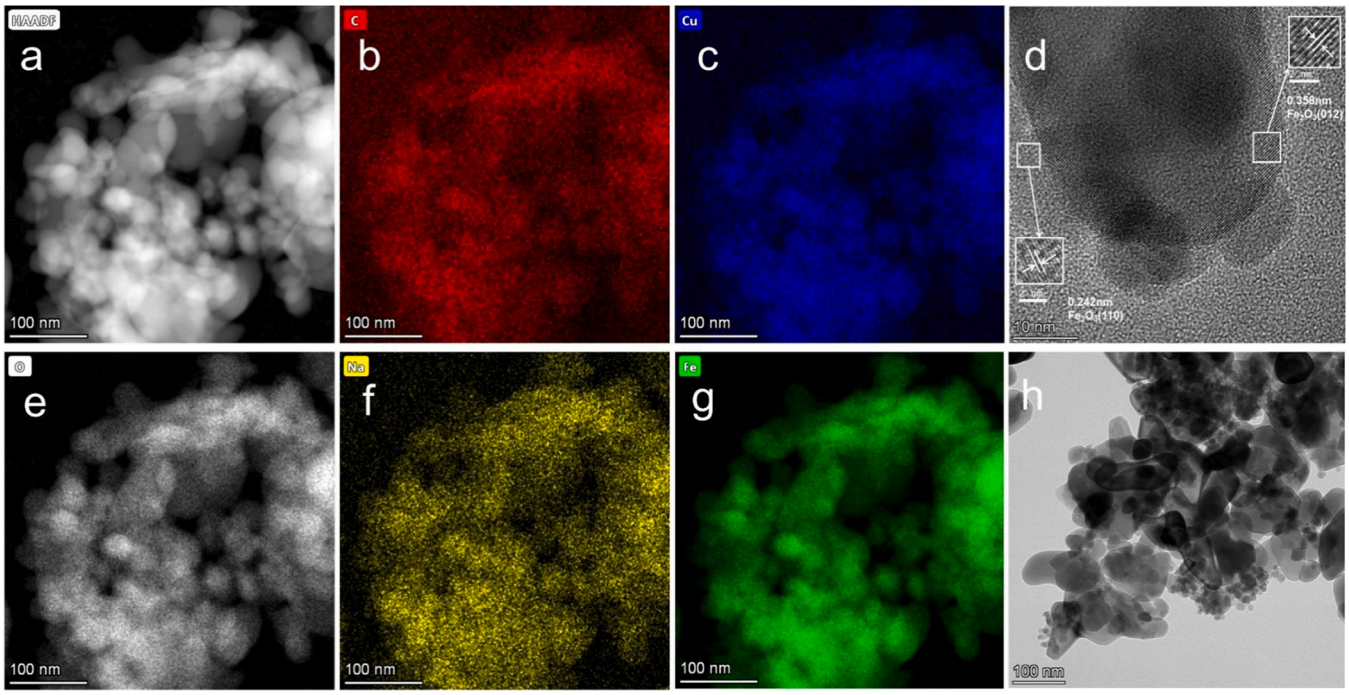

Fig. 2. HAADF-STEM (a) and element mapping of C (b), Cu (c), O (e), Na (f) and Fe (g) and HRTEM (d), TEM (h) of 3-NFC-5 catalyst.

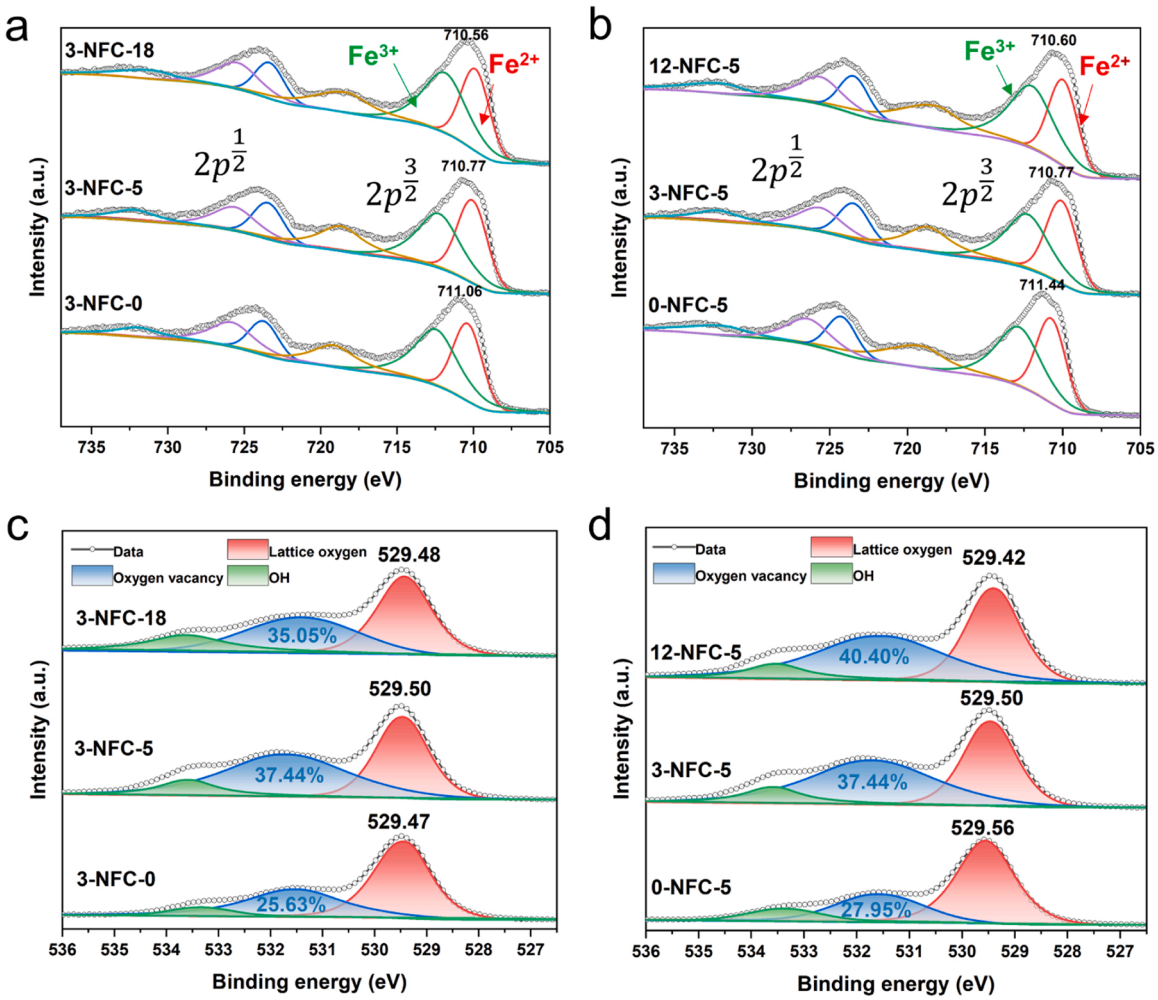

Fig. 3. XPS Fe 2p and O 1s spectra of several y-NFC-5 (a), (c) and 3-NFC-x (b), (d).

from 0-NFC-5–12-NFC-5 (Fig. S7b).

3.3. Aromatics synthesis over y-NFC-x/HZSM-5 bifunctional catalysts

CO_2 hydrogenation to aromatics over y-NFC-x catalysts with various Cu and Na contents was first conducted at 320 °C, 3 MPa and 1500 ml/g_{cat} h^{-1} with a metal oxide/zeolite mass ratio of 1:1 (Fig. 4 and Table S6).

After Cu addition, CO_2 conversion dramatically increased from 36.12% to 42.11% at 0.89% of Cu content, and decrease to about 39% for 1.38% and 2.07% of Cu content, indicating that a slight amount of Cu modification was beneficial to the CO_2 adsorption and activation on the catalyst surface. However, extra Cu modification could probably weaken the reaction activity of FTS according to the increased CO selectivity of 3-NFC-10 and 3-NFC-18, because the increased surface Cu/Fe atomic ratio reduced surface exposed Fe species. Besides, CH_4 selectivity first slightly increased to 8% at 3-NFC-5 due to the intensified H-spillover effect [42] and then maintained at a steady level, suggesting that Cu concentration had tiny influence on CH_4 formation. Likewise, the selectivity of C_2-C_4 paraffins first increased from 6.9% to 9.48% and kept stable at this level. Furthermore, a decrease in aromatics selectivity was observed for 3-NFC-10 and 3-NFC-18.

The lack of Na in the reaction system, however, led to CO_2 conversion as low as 16.62%, while CH_4 selectivity reached to 35.89%. However, CO_2 conversion dramatically increased with the introduction of Na, suggesting that Na played an important role in CO_2 dissociation to CO and further C-C coupling process. Further increasing Na content to 12% led to decreased CO_2 conversion as 34.3%, which could be explained by the increased C/H ratio caused by increased surface basicity. Meanwhile, CO selectivity presented an increasing trend, while CH_4 selectivity showed a substantial decline. C_2-C_4 paraffins, however, slightly increased with the addition of Na, which could be attributed to the enhanced C-C coupling ability provided by Na doping [22]. Aromatics selectivity, besides, exhibited the highest value at 3% Na content (50.68%) and decreased to 35.68% at 12% Na content. However, the ratio of BTX in aromatics gradually increased to 28.36% at 12% of Na content. This phenomenon could be explained by the passivated Brönsted acid sites due to the migration of Na species from iron oxide surface to HZSM-5, poisoning the active sites for aromatization. Meanwhile, the passivated external acid sites alleviated the undesired alkylation of BTX to heavy aromatics [43].

Increasing reaction temperature contributed to drastically elevated CO_2 conversion, which could probably due to the endothermic nature of RWGS, producing considerable CO at high temperature. However, in spite of the strong exothermic property of FTS [44], CO selectivity witnessed a decreasing trend with the increase of temperature. This result could be probably explained by the rapid consumption of olefins intermediate to generate either paraffins or aromatics at higher temperature, thus thermodynamically promoting the FTS reaction. The increased C_2-C_4 paraffins selectivity and decreased aromatics selectivity revealed that hydrogenation of olefins to paraffins was more favorable at high temperature.

Significant increase of CO_2 conversion from 36.94% to 44.58% was observed after reaction pressure was lifted from 1.8 MPa to 3.6 MPa, while CO selectivity underwent impressive decline from 14.9% to 10.65%, suggesting that the molecular-reduced FTS was favorable at higher pressure. The intensified consuming of CO further promoted RWGS according to the Le chatelier's principle [45], boosting CO_2 conversion. Aromatics selectivity gradually increased and maximized at 3 MPa, and further increasing the pressure to 3.6 MPa led to a decrease. The decrease in aromatics selectivity at higher pressure could be attributed to the formation of more saturated hydrocarbons [46], as evidenced by the dramatically enhanced C_{5+} selectivity (24.71%) and C_2-C_4 hydrocarbons selectivity (12.97%) at 3.6 MPa (Table S6).

With the increase of space velocity, CO_2 conversion dropped from 44.17% to 32.83%, while CO selectivity drastically increased to 26.39% at 4000 ml/g_{cat} h^{-1}. Enhanced space velocity could shorten residence time of intermediates on catalyst, which could also be verified by the increase C_2-C_4 olefins selectivity. Nevertheless, the C_{5+} selectivity observed a slight increase at higher space velocity, which could be

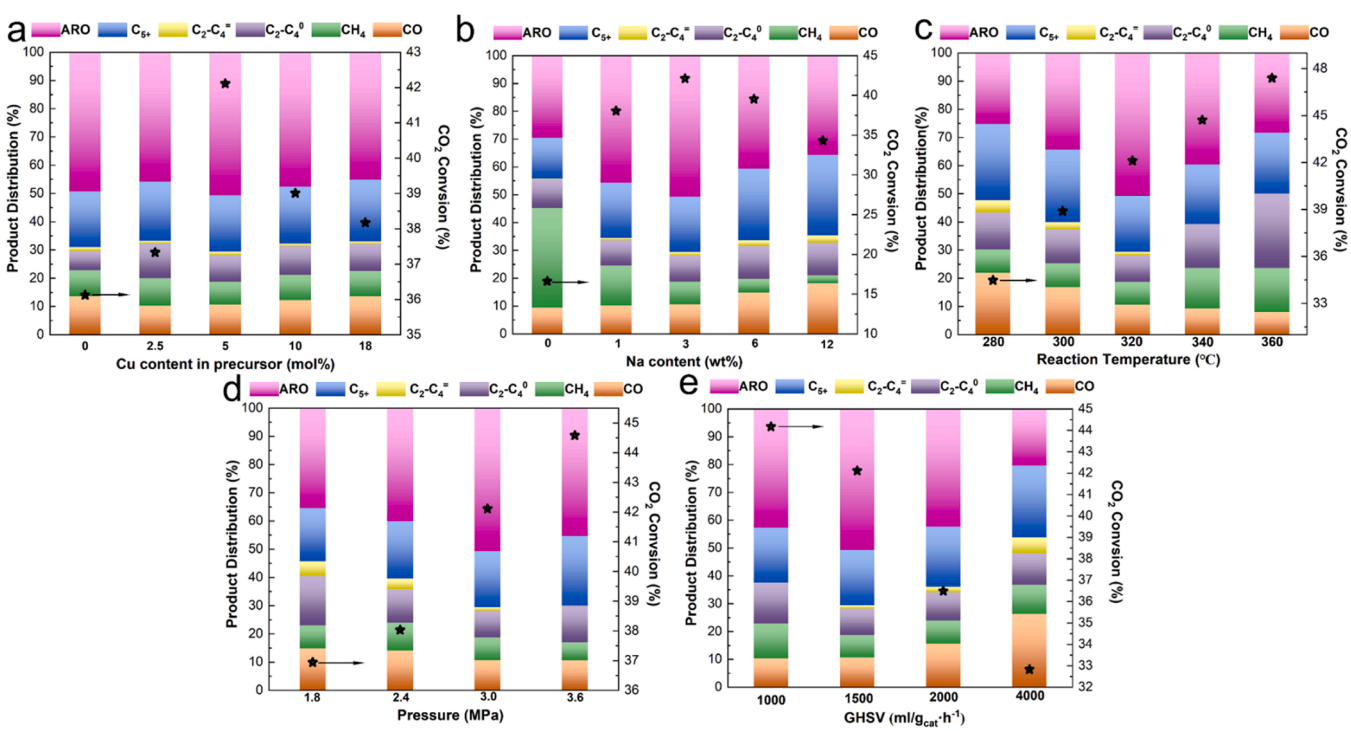

Fig. 4. Catalytic performance of CO_2 hydrogenation over y-NFC-x/HZSM-5 catalyst: CO_2 conversion and product selectivity over y-NFC-x/HZSM-5 catalyst with different Cu content (a), Na content (b) at 320 °C, 3 MPa and 1500 ml/g_{cat} h^{-1}, and effect of reaction temperature (c), reaction pressure (d), space velocity (e) on CO_2 hydrogenation over 3-NFC-5 catalyst. Notes: C_2-C_4^0, C_2-$C_4^=$, C_{5+} and ARO represent C_2-C_4 paraffins, C_2-C_4 olefins, C_{5+} aliphatic and aromatics, respectively.

ascribed to the increased collision probability of CH_x* species, thus forming long chain hydrocarbons. The highest aromatics selectivity (50.68% including CO) was obtained at 1500 ml/g_{cat} h^{-1}.

The long-term stability of 3-NFC-5/HZSM-5 was tested at 320 ℃, 3 MPa and 1500 ml/g_{cat} h^{-1} (Fig. 5b). Both CO_2 conversion and aromatics selectivity only decreased by 3% after 120 h test, while selectivity of other products remained stable, suggesting promising future utilization. The NH_3-TPD of HZSM-5 before and after stability test (Fig. S8 and Table S7) indicated the decrease of density of medium strong acid sites, which was considered crucial for aromatization [5], from 1.94 to 1.23 mmol/g, agreeing well with the slightly passivated aromatics selectivity.

In conclusion, CO_2 hydrogenation over 3-NFC-5/HZSM-5 catalyst achieved 42.11% CO_2 conversion and 50.68% total aromatics selectivity with a high aromatics' yield of 21.3% and BTEX yield of 13.8% (including CO) (Table S1), ranking among the best in the recently published literature.

3.4. Synergistic effect of Cu and Na on Fe-based catalyst

3.4.1. CO_2 hydrogenation performance over sole y-NFC-x catalysts

In order to investigate the synergistic effect of Cu and Na, CO_2 hydrogenation performances on 0-NFC-0, 3-NFC-0, 0-NFC-5 and 3-NFC-5 were first compared (Fig. 5a and Table S6). Single modification of Cu on Fe-based catalysts slightly increased CO_2 conversion from 17.97% to 21.94%, while CO selectivity was suppressed around 4%. It is worth mentioning that C_2-C_4 olefins were nearly not detected without the addition of Na, while Cu addition inhibited the formation of C_2-C_4 paraffins and C_{5+} hydrocarbons simultaneously, along with the drastically enhanced CH_4 selectivity, suggesting that Cu passivated the C-C coupling process and accelerated hydrogenation capability. Besides, simple Na modification dramatically elevated the CO_2 conversion to 41.99%, while the formation of undesired CH_4 and C_2-C_4 paraffins were significantly prevented. Conversely, selectivity of C_2-C_4 olefins was sharply enhanced to 28.68% because of the high surface C/H ratio caused by the strengthened CO_2 adsorption ability, which was generated by the increased surface basicity provided by Na addition. For the Na-Cu co-modified catalyst (3-NFC-5), surprisingly, CO_2 conversion observed a slight promotion compared with 3-NFC-0. Moreover, the C_2-C_4 olefins selectivity was further boosted to 34.09% with the sacrifice of C_{5+} selectivity to 28.18% (Fig. 5c). However, the co-existence of Cu and Na just slightly increased CH_4 selectivity from 12.03% to 12.98%, which contrasted fiercely with the Na-absent case. The discussed results confirmed the synergistic effect of Na and Cu on light olefins production, which deserved deeper research.

3.4.2. Reduction behavior

H_2-TPR was employed to study the reduction behavior of Fe-based catalysts (Fig. 6a). For the pure 0-NFC-0 catalyst, the peak located at 306 ℃ represents typical reduction of bulk Fe_2O_3 to Fe_3O_4, while two overlapping peaks at about 520 ℃ and 687 ℃ could be attributed to sequential transformation of bulk Fe_3O_4 to FeO and FeO to Fe [47]. With Cu promotion, the reduction peak of bulk Fe_2O_3 to Fe_3O_4 significantly shifted to 234 ℃, while a new peak displayed at 133 ℃, which could be explained by the reduction of small CuO clusters without interaction with bulk Fe_2O_3 [48]. Moreover, the two overlapped peaks on behalf of deep reduction of Fe species shifted slightly to lower temperature, suggesting that Cu doping facilitated the reduction of Fe. For 3-NFC-0, all three peaks shifted to higher temperature, indicating that the suppression of H_2 adsorption on Na-rich surface retarded reduction of Fe.

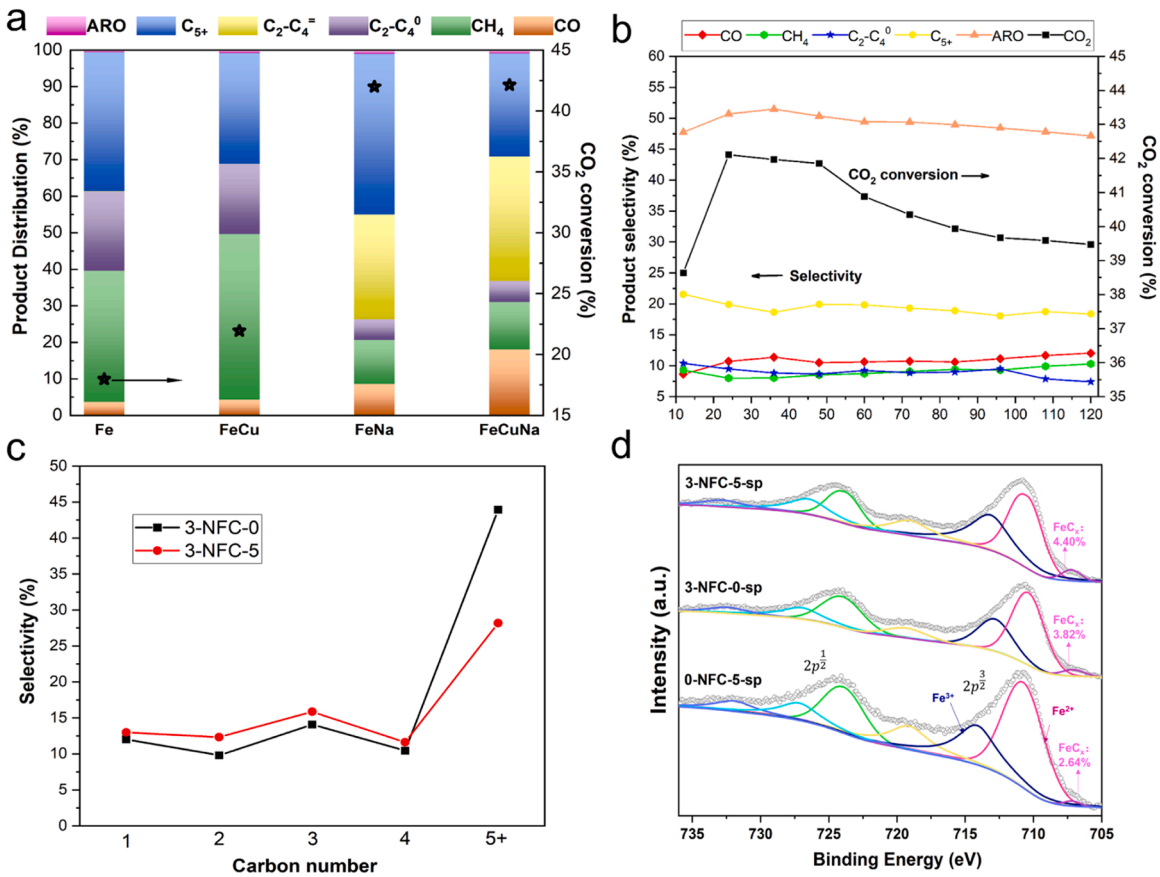

Fig. 5. Catalytic performance of CO_2 hydrogenation over y-NFC-x catalysts at 320 ℃, 3 MPa and 1500 ml/g_{cat} h^{-1} (a), and the effect of Cu on carbon number distribution for CO_2 hydrogenation over y-NFC-x catalyst (c), 120 h stability test for CO_2 hydrogenation over 3-NFC-5/HZSM-5 catalyst at 320 ℃, 3 MPa and 1500 ml/g_{cat} h^{-1} (b) and the Fe 2p XPS spectra of spent catalysts after aromatization test (d).

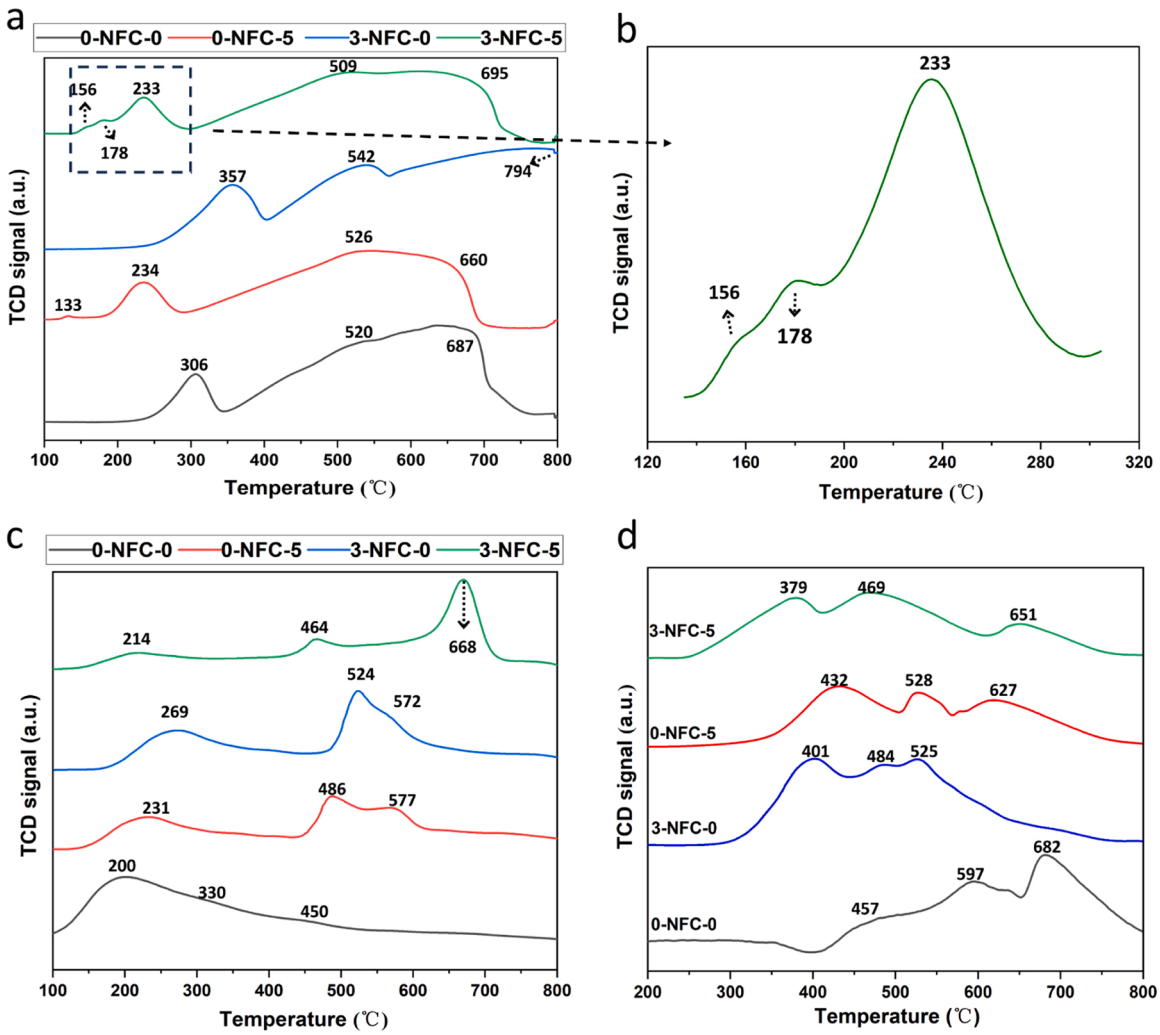

Fig. 6. H_2-TPR (a), detailed H_2-TPR of 3-NFC-5 (b), CO_2-TPD (c) and CO-TPR (d) spectra of several y-NFC-x catalysts.

For the Na and Cu co-promoted 3-NFC-5, surprisingly, Cu reduction peak split into two peaks corresponding to CuO clusters interacting weakly and strongly with Fe_2O_3 (Fig. 6b) [49]. In contrast to the successive reduction peaks of CuO and Fe_2O_3 in 0-NFC-5, the overlapped peaks displayed synchronous reduction of CuO and Fe_2O_3, further convincing that Na addition intensified Cu-Fe interaction. Moreover, it is generally accepted that Cu accelerates H_2 activation and transformation through H spillover effect, while Na doping increase surface basicity which inhibits H_2 adsorption [10]. Therefore, it could be speculated that Na addition decrease the nearby activation of H species, thereby neutralizing the strong reduction ability of 0-NFC-5 catalyst. XRD patterns of reduced 3-NFC-5 (Fig. S9) showed more distinct Fe_3O_4 diffraction peak than 0-NFC-5 and less distinct peaks than 3-NFC-0, agreeing well with TPR results.

3.4.3. CO_2 adsorption and activation

It is widely acknowledged that oxygen vacancies on Fe_3O_4 phase plays a crucial role in CO_2 adsorption, activation and hydrogenation to produce CO through RWGS [17]. Thereby, the formation energy (FE) of surface O_v on different modified Fe-based catalyst was calculated by DFT methods. As is illustrated in Fig. S10, with the absence of Na, the formation energy of surface oxygen vacancy over pure Fe_3O_4 and Cu-modified Fe_3O_4 was 1.85 eV and 1.81 eV respectively, with a deviation of 0.04 eV, suggesting Cu addition could promote the formation of oxygen vacancy over Fe_3O_4. After Na promotion, the O_v formation energy increased to 2.24 eV on Na-Fe_3O_4. After Cu and Na co-modification, the O_v formation energy decreased to 2.17 eV. The difference of O_v formation energy after adding Cu on Na-pretreated Fe_3O_4 and Na-absence Fe_3O_4 was 0.07 eV and 0.04 eV, respectively. Thus, it could be ratiocinated that Cu modification on Na-Fe_3O_4 facilitated the formation of oxygen vacancy to a greater extent. Coincidentally, the TPR results displayed consistent trend that, the reduction temperature of Fe_2O_3 to Fe_3O_4 on Na-containing and Na-absent Fe catalysts witnessed a decrease of 124 ℃ and 72 ℃ after Cu doping, respectively, indicating that the H-spillover effect of Cu addition was more remarkable on Na-doping surface, thereby removing more surface O atoms and creating more O_v. These results provided extra evidences for the existence of synergy effect between Cu and Na on surface O_v formation during reduction process.

CO_2 adsorption properties on active sites were further studied by CO_2-TPD-MS. As is shown in Fig. 6c, Table S8 and Fig. S11, all catalysts displayed three major peaks which could be classified as weak, medium strong and strong CO_2 adsorption state. The weak and medium strong sites could be attributed to physical and chemical adsorption over active sites [50], while the strong adsorption sites are related to the adsorption of CO_2 on O_v-related active sites [51]. For sole Fe catalyst, only CO_2 desorption peaks below 450 ℃ could be observed, and the peak area proportion of weak adsorption was high as 49.25%, suggesting the priority for physical CO_2 adsorption over sole Fe catalyst. The medium strong and strong adsorption sites occupied 28.41% and 20.34% respectively, reflecting the poor CO_2 adsorption and activation ability. After Cu modification, all desorption peaks shifted to higher

temperature, the weak adsorption area decreased to 33.55%, while the area for strong adsorption increased to 35.83%. Combining with the increased CO_2 conversion (Fig. 5a) and decreased O_v formation energy, it is speculated that Cu addition increased surface O_v amount, providing more strong active sites for CO_2 adsorption. At meantime, the increased amount of medium strong site could be attributed to the increased surface basicity caused by electron donating of Cu to Fe, improving CO_2 adsorption [17]. For Na-modified Fe, the medium strong site shifted from 486 ℃ to 524 ℃ with an increase in peak area of 8%, suggesting Na provides more election-rich surface compared with Cu. However, the peak area of strong adsorption decreased from 35.83% to 17.37%, indicating the reduced amount of O_v, which was in accordance with the increased O_v formation energy after Na modification. For Cu and Na co-modified Fe, the strong adsorption peak drastically shifted to 668 ℃, indicating the strengthened CO_2 adsorption intensity. Thus, the unique O_v-participating CO_2 adsorption on Fe surface with co-decoration of Na and Cu needed further clarification.

In order to uncover the intermediates for CO_2 activation, *In situ* DRIFTS analysis was conducted on the reacted catalysts to further reveal the nature of CO_2 adsorption state. Fig. 7a illustrated the *In situ* DRIFTS spectra of 0-NFC-5 within the range of 1000–1800 cm^{-1}. IR bands correlated with adsorbed CO_2 (1253 cm^{-1}), monodentate carbonate (1320 cm^{-1}) and bidentate carbonate (1295 cm^{-1}) could be observed [52–54]. Moreover, peaks related to surface HCO_3* also appeared at 1699 cm^{-1} [55]. In addition, peaks belong to surface COOH* (1147 cm^{-1}, 1432 cm^{-1} and 1775 cm^{-1}) [56–58] and HCOO* (1371 cm^{-1} and 1542 cm^{-1}) [52] appear simultaneously at 5 min on stream. However, the intensity of surface COOH* characteristic peaks remained stable during the whole test, while surface HCOO* was drastically enhanced and remain stable after 10 min on stream, unveiling that surface HCOO* predominates as the main intermediate during CO_2 activation. Meanwhile, peaks assigned to surface CH_xO* species, which was considered as the intermediate for CH_4 formation [59], could be observed between 1000 and 1100 cm^{-1} [60]. For 3-NFC-0 (Fig. 7b), peaks belonging to adsorbed CO_2 at 1253 cm^{-1} could also be observed and weakened during the test. Conversely, compared with 0-NFC-5, only the monodentate CO_3^{2-} could be detected at 1319 cm^{-1}. Besides, intensity of surface COOH* species (1147, 1421, 1770 cm^{-1}) was observed on 3-NFC-0 and continuously reinforced during the test. In addition, surface HCOO* (1390, 1561, 1578 and 1610 cm^{-1}) [52,61,62] could also be observed. For 3-NFC-5 (Fig. 7c), similar case could be summarized for the co-existence of COOH* and HCOO*. However, inconsistent with 3-NFC-0, surface HCOO* at 1548 and 1578 cm^{-1} was detected, while the peaks at 1390 and 1610 cm^{-1} were not observed. Moreover, it is worth mentioning that the intensity of surface COOH* surpass that of surface HCOO* on 3-NFC-5, while 3-NFC-0 displayed the converse trend, suggesting that Cu modification on FeNa catalyst enhance the formation of COOH*.

DFT Bader charge analysis (Fig. 8c, d and Table S9) further demonstrated that the adsorbed CO_2 was more electronically polarized on Cu and Na co-decorated Fe_3O_4 (111) surface, as evidenced by the increased Bader charge of carbon atom. Therefore, the weakened electron density on carbon atom enhanced its capture possibility on the basic catalyst surface, generating more surface COOH* species.

As is reported in previous studies [63,64], both surface HCOO* and COOH* could be the precursor for further evolution. COOH* leads to direct splitting for the formation of surface CO* and OH*, whereas HCOO* transforms sequentially as HCOO*→HCOOH*→HCO*, then surface HCO* could be hydrogenated either to CH_3O* or to HCOH* for further transformation. In summary, for Fe-based catalyst with sole Cu modification, HCOO* was responsible as the major intermediate for CO_2 activation. For Na and Na and Cu co-modified catalyst, both HCOO* and COOH* were detected, suggesting that Na was crucial for COOH* formation. Besides, the COOH* intensity was stronger on Na and Cu co-modified catalyst, which promoted CO formation through breakage of C-O bond. Thus, surface COOH* may probably act as the potential provider of CO species. Hence, CO activation was further studied.

3.4.4. CO activation and carburization behavior

As is shown in Fig. S12, the *In situ* DRIFTS spectra of 0-NFC-5, 3-NFC-0 and 3-NFC-5 between 1800 and 2200 cm^{-1} illustrated the adsorption state of CO. For 0-NFC-5, weak peaks located at 2175 and 2110 cm^{-1} belong to gaseous CO (CO (g)) [58], while the peak at 1980 cm^{-1} was assigned to bridge-bonded CO (CO (b)) [65]. CO (g) peak was slightly

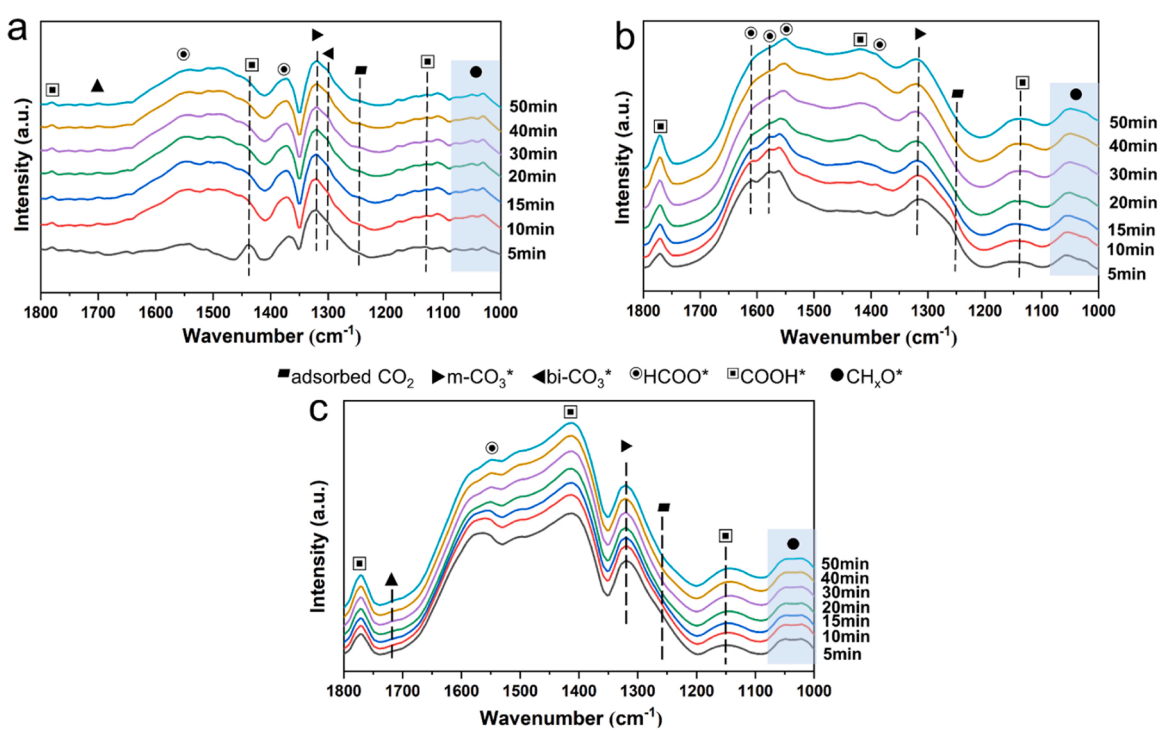

Fig. 7. *In situ* Drifts spectra between 1000 and 1800 cm^{-1} of 0-NFC-5 (a), 3-NFC-0 (b) and 3-NFC-5 (c) under reaction gas at 320 ℃ and ambient pressure.

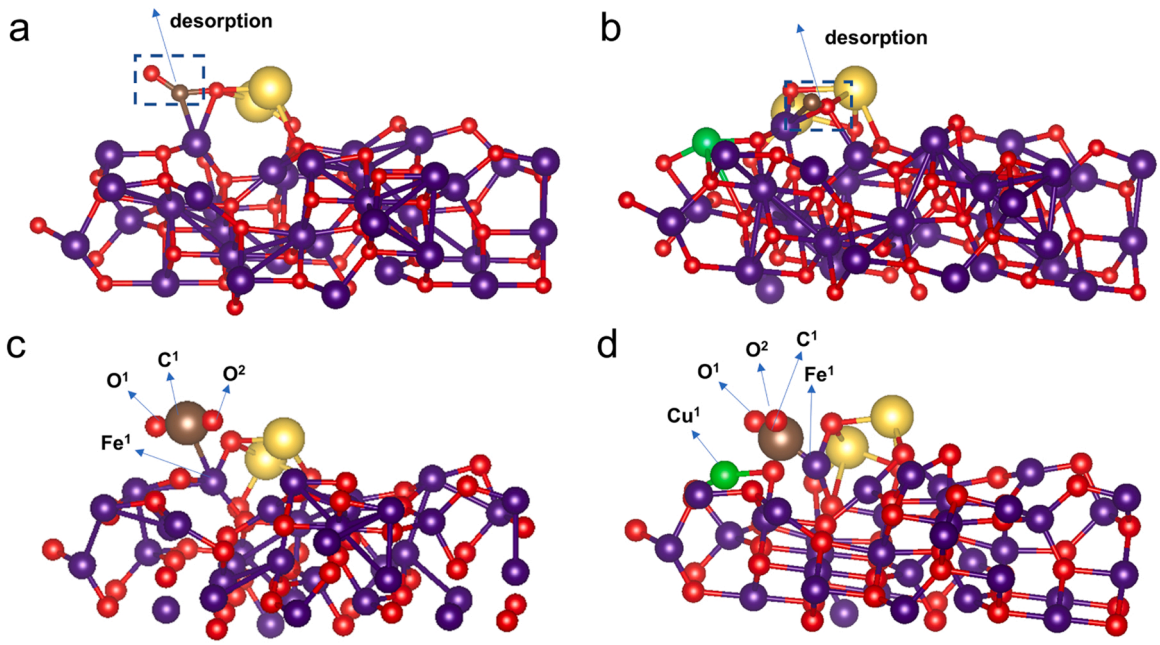

Fig. 8. CO desorption model on Na and Na-Cu co-modified Fe_3O_4 (111) surface (a) and (b); CO_2 adsorption model on Na and Na-Cu co-modified Fe_3O_4 (111) surface (c) and (d); Notes: Na decoration was applied in the form of Na_2O. The atom color and corresponding element was iron (purple), copper (green), sodium (yellow), carbon (brown) and oxygen (red).

enhanced at the beginning of the test and maintained through almost the whole test. Besides, the gradually receding peak at 1980 cm^{-1} suggested that bridge-bonded CO was continuously consumed during the test. For the spectra of 3-NFC-0, CO (g) was also witnessed, while peaks representing CO (b) was almost invisible. Surprisingly, the peak located at 2040 cm^{-1} on behalf of the linear-adsorbed CO (CO (l)) was observed [66]. For 3-NFC-5, CO (g) at 2180 and 2110 cm^{-1}, CO (l) at 2140 cm^{-1} and CO (b) at 1975 cm^{-1} could all be observed in the spectra. However, the CO (b) and CO (l) peak emerged and maintained the stable intensity during the test, reflecting a sharp contrast with the CO (g) peak, which experienced continuous intensification through the test. Thereby, it is speculated that the CO adsorbed on the active sites of 3-NFC-5 could more easily desorb from the surface and release into the gas phase, which was in accordance with the highest CO selectivity generated on 3-NFC-5 catalyst.

Furthermore, CO/H_2-TPSR (Fig. 9) was carried out on the reacted catalyst to further unveil the surface activation and reaction of CO. The MS spectra of $m/z = 16$, 27, 28 and 30 was assigned to methane, C_2 olefins, CO and C_2 paraffins. Moreover, the methane and CO spectra imply the dissociative adsorption and non-dissociative adsorption of CO [60]. The $m/z = 16$ spectra illustrated the increasing temperature of 490 ℃, 506 ℃ and 532 ℃ of the major peak for 0-NFC-5, 3-NFC-5 and 3-NFC-0, suggesting that CO dissociative adsorption tendency decreases as 0-NFC-5 > 3-NFC-5 > 3-NFC-0, which agreed well with the peaks of bridge-bonded CO observed in DRIFTS spectra for 0-NFC-5 and 3-NFC-5, but invisible in 3-NFC-0 spectra, as bridge-bonded CO is considered directly related with CO dissociation [67]. For the $m/z = 28$ spectra representing non-dissociative CO, 0-NFC-5 exhibited faint intensity compared with 3-NFC-5 and 3-NFC-0, suggesting the negligible amount of non-dissociative CO, which not only fitted well with invisible CO (l) and weak CO (g) peaks in 0-NFC-5 DRIFTS spectra, but also verified its ultra-low CO selectivity in CO_2 hydrogenation reaction. Meanwhile, the CO desorption area increases drastically after Na doping, suggesting the enhanced capacity of CO non-dissociative activation. For 3-NFC-0, the major peak located at 593 ℃ was witnessed, which was higher than that in 3-NFC-5 (516 ℃). The temperature discrepancy implied that CO desorption was easier on 3-NFC-5, which was highly in accordance with the more distinct CO (g) peaks in DRIFTS spectra of 3-NFC-5 compared with 3-NFC-0. In addition, the relative content of the CO dissociative and non-dissociative activation was quantitatively analyzed by the total area ratio of $m/z = 16$ and 28 spectra ranging between 100 ℃ and 800 ℃, which is listed in Table S6. Intuitively speaking, 0-NFC-5 exhibited the highest proportion of dissociative CO, while 3-NFC-0 only possessed a tenth of that for 0-NFC-5. After Cu modification, the value further declined to 0.013 for 3-NFC-5, indicating the least active sites for CO dissociative activation. DFT calculation of CO desorption from decorated Fe_3O_4 (111) surface (Fig. 8a-b and Table S11) further indicated that CO desorption energy barrier was lower on 3-NFC-5, fitting well with the experimental results.

In summary, CO non-dissociative activation could be improved after co-modification by Na and Cu. For dissociative activation, virtually, the adsorbed CO species could either undergo direct heterolytic cleavage into C* and O*, where the former could further transform into surface CH_x*, or convert following the sequence as CO*→HCO*→HCOH*→CH*+OH* with the assistance of H species for further reaction [63]. Thus, the intensified non-dissociative activation of CO signifies less amount of surface CH_x species on 3-NFC-5. However, the sole 3-NFC-5 catalyst exhibited highest C_2-C_4 olefins selectivity and lowest C_{5+} selectivity (Fig. 5a and Table S6), suggesting the unique and efficient C-C coupling ability for favorable C_2-C_4 olefins formation. Thus, the C-C coupling properties of Fe-based catalysts were further investigated.

3.4.5. Co-promotion of Cu and Na in C-C coupling process

CO dissociative activation provides surface CH_x* as a crucial intermediate for FTS, which could be further hydrogenated to CH_4, or undergo chain propagation to form surface C_xH_y* species. *In situ* DRIFTS between 2650 and 3250 cm^{-1} (Fig. S13) indicated the existence of CH_4 at 3000 cm^{-1} for all three catalysts [59]. However, C-H vibration of alkenes at 3050 cm^{-1} [54] was invisible for 0-NFC-5 but appeared for 3-NFC-5 and 3-NFC-0, meanwhile, C-H vibration for alkanes at 2960 cm^{-1} [54] appeared for 0-NFC-5, indicating that the absence of Na led to unfavorable hydrogenation of alkenes to alkanes. Besides, the C-H vibration for 3-NFC-5 and 3-NFC-0 was undetected because of the coverage of HCOO* species appeared around 2800–3000 cm^{-1} [68].

TPSR spectra of $m/z = 27$ and 30 represent unsaturated C_2H_3 and

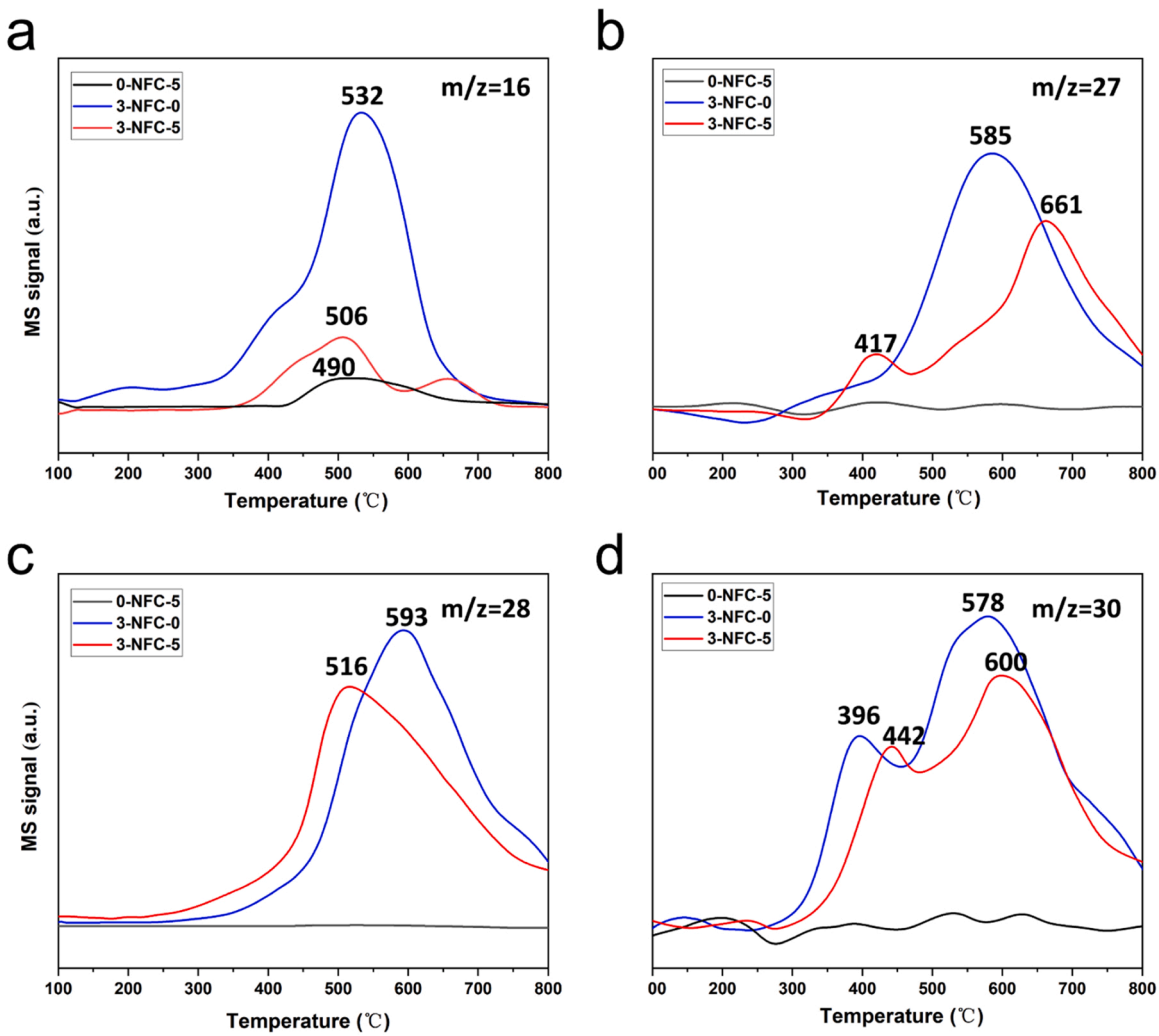

Fig. 9. CO pre-adsorbed H_2-TPSR spectra of $m/z = 16$ (a), $m/z = 27$ (b), $m/z = 28$ (c) and $m/z = 30$ (d) on various y-NFC-x catalysts.

saturated C_2H_6 species (Fig. 9b, d), while the ratio of total area of aforementioned C_2H_3 and C_2H_6 curves ranging between 100 and 800 ℃ was 0.452, 0.944 and 0.762 for 0-NFC-5, 3-NFC-0 and 3-NFC-5 (Table S10), respectively. The maximal value of 3-NFC-0 indicated that the poorest H_2 activation capability, that is probably because of the strong basicity caused by Na elevated surface C/H ratio, thereby producing more olefins. The enhanced H_2 activation after Cu doping increases surface H proportion, hydrogenating olefins to paraffins. Without Na modification, the H-spillover effect was dominated, creating minimum C/H ratio, which distinctly explained the highest CH_4 and C_2-C_4 paraffins selectivity for 0-NFC-5. As a result, Na could neutralize the strong H_2 activation ability of Cu, preventing undesirable further hydrogenation of surface C_xH_y* species. The ratio of (c+d)/a listed in Table S10 represents the relative concentration of C_1 and C_2 hydrocarbons obtained in TPSR spectra, which reflects the C-C coupling ability to form C_2 hydrocarbons. The ratio varies in descending order as 3-NFC-5 > 3-NFC-0 > 0-NFC-5, suggesting that C_2 hydrocarbons are easiest to form on Na and Cu co-modified Fe. At meantime, the comparatively low value of (c+d)/a could be explained by stronger C-C coupling ability, generating heavier hydrocarbons that are not detected in the spectra. Besides, 0-NFC-5 exhibits minimum value of 0.051, indicating that Na plays an indispensable role in C-C coupling for chain propagation.

Thus, CO-TPR accompanied with $m/z = 44$ (CO_2) MS spectra was conducted on y-NFC-x catalysts to study the carburization behavior of various modified Fe-based catalysts (Figs. 6d and S14). All the catalysts were in-situ reduced in H_2 flow for 2 h before tests. Typically, 3 major peaks located between 300 and 700 ℃ could be observed for all 4 catalysts. Previous study has proved that Fe phase was more easily to be carbonized than Fe_3O_4 phase [68]. Thus, combining with XRD of reduced y-NFC-x that displayed Fe and Fe_3O_4 as the main phase (Fig. S9) and XRD of reacted catalysts that demonstrated χ-Fe_5C_2 as the major phase (Fig. S15), it could be speculated that the first peak represented the carburization of Fe phase to χ-Fe_5C_2, while the second peak belonged to carburization of Fe_3O_4 phase. Compared with other 3 catalysts, 0-NFC-0 displayed highest carburization temperature for those peaks, while adding Cu and Na alone could both enhance the carburization behavior, as evidenced by the decreased temperature, and Na improved it to a larger extent. Compared with 3-NFC-0, these two peaks shifted from 401 ℃ and 484–379 ℃ and 469 ℃, respectively for 3-NFC-5, further indicating that Cu could facilitate the carburization of Fe species, providing more active sites for C-C coupling. This conclusion could be further clarified by MES spectra of spent 3-NFC-0 and 3-NFC-5 after CO_2 hydrogenation without HZSM-5 presence (Fig. S16 and Table S12), where the former possessed Fe_3O_4 and χ-Fe_5C_2, while the latter witnessed pure χ-Fe_5C_2 phase. However, 0-NFC-5 without Na showed peaks at higher temperature than 3-NFC-5 in CO-TPR profile, suggesting the poor carburization ability with the absence of Na, leading to decrease of active sites and olefins generation. The third peak at highest temperature could be attributed to the deep carburization of χ-Fe_5C_2 to carbon-rich carbide phases like Fe_7C_3 at high temperature [44], which was less active site for FTS compared with χ-Fe_5C_2 [22], while χ-Fe_5C_2 was widely validated as active sites for light olefins formation [47]. The

high temperature peak of 3-NFC-5 at 651 ℃ reflected that Cu could retard the formation of carbon-rich Fe species, generating more χ-Fe_5C_2 for light olefins production.

3.5. Characterization of the spent catalysts

XRD of spent 3-NFC-x (Fig. S15) after aromatization all displayed characterization peaks of χ-Fe_5C_2 and Fe_3O_4 phase, while 3-NFC-5 displayed more distinct χ-Fe_5C_2 phase, indicating highest content of χ-Fe_5C_2 in 3-NFC-5 (Fig. S15b), agreeing well with the CO-TPR results. Fig. S17 showed XRD patterns of spent 0-NFC-0, 3-NFC-0, 0-NFC-5 and 3-NFC-5. χ-Fe_5C_2 and Fe_3O_4 phase could be observed in 3-NFC-0 and 3-NFC-5, but 0-NFC-0 and 0-NFC-5 displayed Fe_3O_4, Fe and Fe_3C phase. The presence of Fe further confirmed the poor carburization ability without Na. While carbon-poor phase Fe_3C was considered less active for FTS reaction compared with Fe_5C_2 [69], leading to higher CH_4 selectivity and lower C_{2+} hydrocarbons selectivity compared with Na-present case (Fig. 5a). Besides, Fe 2p XPS curve (Fig. 5d) of spent catalysts illustrated surface iron carbides at about 707 eV [22]. 3-NFC-5 witnessed highest surface iron carbides proportion of 4.40% compared with 3-NFC-0 and 0-NFC-5.

Fig. S18 displayed TEM and HRTEM of spent 3-NFC-0 and 3-NFC-5. It could be observed that a carbon layer existed after 24 h of reaction on spent 3-NFC-0 (Fig. S18b), which was invisible on spent 3-NFC-5 (Fig. S18d), suggesting that Cu could prevent the carbon deposition and maintain the catalyst stability, as reported by previous study [70]. Furthermore, HRTEM of spent 3-NFC-5 showed the lattice fringes of 0.203 nm and 0.254 nm, belonging to the Fe_5C_2 (510) and Fe_3O_4 (310) lattice plane [10], fitting well with the XRD of the spent 3-NFC-5 (Fig. S15).

3.6. Elucidating and summarizing the role of Na and Cu in Fe-based catalysts

Na acted as the basement of the reaction system, and its roles are summarized as follows: (1) Na was crucial for the adsorption of CO_2 on Fe-based catalysts, as evidenced by the dramatically increased CO_2 conversion from 16.62% to 42.11% for 0-NFC-5 and 3-NFC-5, and the peak shifted to higher temperature after Na doping in CO_2-TPD (Fig. 6c). (2) As proved by the *In situ* DRIFTS (Fig. 7), Na was important for the formation of COOH* intermediates, which acted as the precursor of CO through RWGS. (3) Na dramatically proved the non-dissociative activation of CO (Fig. S12 and Fig. 9). (4) From CO-TPR results (Fig. 6d), Na decoration facilitated the carburization of Fe-based catalysts, favoring the formation of χ-Fe_5C_2 as active sites for FTS and C-C coupling, which was also proved by CO/H_2-TPSR results of $m/z = 16$, 27 and 30 (Fig. 9 and Table S10). (5) Na could suppress the secondary hydrogenation of lower olefins, avoiding the excessive production of paraffins byproducts, which could also be proved by the dramatically decreased CH_4 selectivity from 45.33% to 12.98% and drastically increased C_{2-4} olefins selectivity from 0.07% to 34.09% after Na modification (Table S6).

The synergistic effect of Cu addition in Na pretreated Fe based catalysts are as follows: (1) According to the H_2-TPR (Fig. 6a) and calculated oxygen vacancy formation energy (Fig. S10), the H-spillover effect of Cu addition was more remarkable on Na-doping surface, thereby removing more surface O atoms and creating more O_v. (2) Cu doping on 3-NFC-0 further enhance the content of COOH* intermediates (Fig. 7). (3) Cu addition on 3-NFC-0 further promote the non-dissociative activation of CO (Figs. 9, S11 and Table S10), producing more gaseous CO and reducing the surface CH_x* content. Thus, excessive C-C coupling could be avoided for more lower olefins production. (4) Cu addition on 3-NFC-0 facilitated the carburization to χ-Fe_5C_2 and retarded the deep carburization to carbon-rich iron carbides, generating more light olefins production.

3.7. Discussion of the mechanism of CO_2 hydrogenation over CuNa co-modified Fe based catalyst

The mechanism of CO_2 hydrogenation over Fe-based catalysts is illustrated in Scheme 1. Generally, CO_2 was adsorbed on the Fe-based catalyst to form surface m-CO_3^{2-} and bi-CO_3^{2-}, followed by transformation into COOH* and HCOO*. COOH* leads to direct formation of surface CO* and OH*, whereas HCOO* transforms sequentially as HCOO*→HCOOH*→HCO*, then surface HCO* could be hydrogenated either to CH_3O* or to HCOH*. CH_3O* was the direct precursor of undesirable CH_4, while HCOH* could ulteriorly transfer into OH* and CH* and participate into chain propagation process. For the CO species derived from COOH*, dissociative and non-dissociative activation could occur in the meantime. Dissociative activation leads to C-O bond heterolysis to generate surface C* and CH_x* species through further hydrogenation, while non-dissociative activation produces gaseous CO by desorption from the surface. For 0-NFC-5, the major active intermediate was confirmed as HCOO*, which was responsible for the favored CH_4 formation through hydrogenation of CH_3O* intermediate. The C_2-C_4 paraffins and C_{5+} generated on 0-NFC-5 could be explained by C-C coupling of CH_x* species formed through HCOO* pathway. Besides, strong H activation triggered by Cu modification resulted in low o/p ratio. After Na modification, surface COOH* observed drastic enhancement. For 3-NFC-0 and 3-NFC-5, HCOO* and COOH* evolution pathway coexist in the reaction system, where surface HCOO* intensity was almost equivalent with that of COOH*, indicating that CH_x* derived from HCOO* and COOH* pathway account for approximate proportion among the reaction intermediates. Combining with the relatively stronger CO dissociative activation capacity on 3-NFC-0, it could be speculated that CO was easier to be activated to CH_x* species on 3-NFC-0, thereby creating CH_x*-rich surface, which was crucial for C-C coupling. Nevertheless, the intensity of COOH* surpassed that of HCOO* on 3-NFC-5, generating more surface adsorbed CO. With the assistance of stronger CO non-dissociative activation, less CO undergoes C-O breakage to produce CH_x*, thereby inhibiting excessive C-C coupling to form long chain hydrocarbons due to the restrained surface CH_x* concentration. Meanwhile, Na addition significantly suppressed further hydrogenation of C_xH_y* species to CH_4 and paraffins, guaranteeing the high yield of light olefins and the tandem formation of aromatics on HZSM-5. Finally, Cu retards the transformation of active χ-Fe_5C_2 into inert Fe_7C_3, thus FTS activity was sustained.

4. Conclusion

CO_2 hydrogenation to aromatics was implemented over a multifunctional catalyst comprising of Cu and Na doped Fe-based catalyst derived from modified MIL-101(Fe) and HZSM-5. The optimal catalytic performance of 42.11% CO_2 conversion and 50.68% aromatics selectivity was achieved over 3-NFC-5/HZSM-5 at 320 ℃, 3 MPa and 1500 ml/$g_{cat}^{-1}h^{-1}$. The synergistic promotion of Na and Cu on light olefins production was responsible for the excellent aromatics selectivity. Through multiple characterizations and DFT calculation, it was found Na worked as the basement of the reaction system by enhancing CO_2 adsorption and facilitating formation of iron carbides. that H-spillover effect promoted by Cu was more remarkable on Na-doping Fe-based catalysts, generating more oxygen vacancies for CO_2 adsorption and activation. Besides, Na was crucial for the formation of COOH* intermediates, and its concentration could be further enhanced after Cu modification. Promoted CO non-dissociative activation after Cu doping on Na-modified Fe catalyst inhibited the formation of CH_x*-rich surface. Combining with the increased content of χ-Fe_5C_2 after Cu doping, restriction of C-C coupling towards C_2-C_4 hydrocarbons was realized. Finally, Na prevented the secondary hydrogenation of olefins to paraffins, boosting light olefins production to the greatest extent. This work extended the understanding of synergistic promotion of Na and Cu on Fe-based/zeolite multifunctional catalysts, promoting aromatics

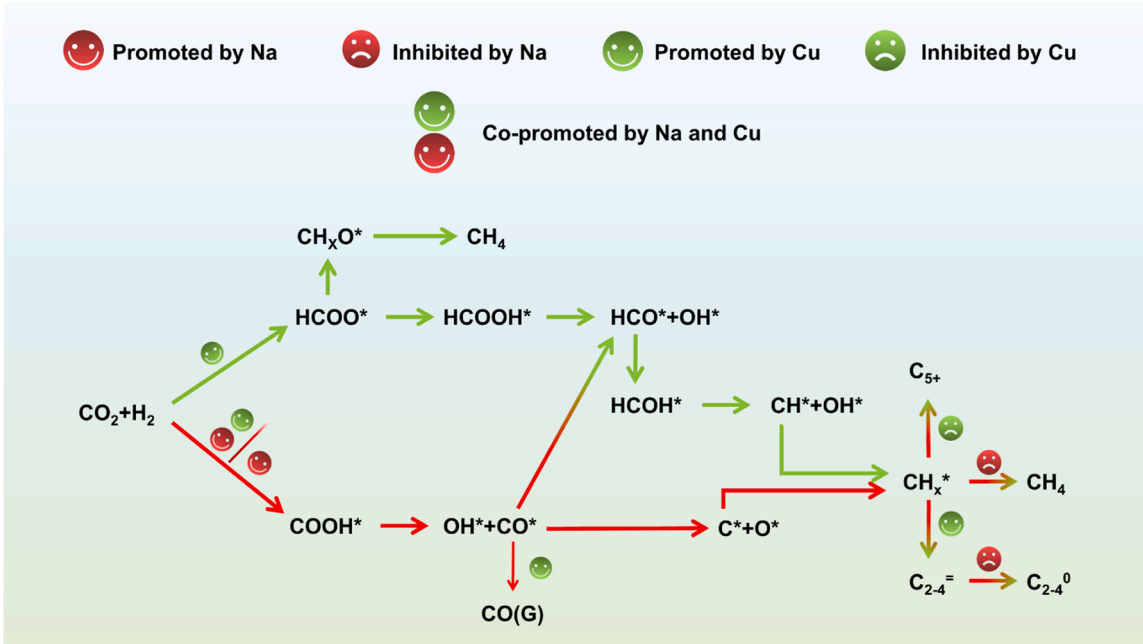

Scheme 1. Mechanism of Na and Cu decoration on CO_2 hydrogenation over Fe-based catalysts.

production. Further research could focus on the revealing of regional interaction between active sites of serial reactions for aromatics production.

CRediT authorship contribution statement

Chonghao Chen: Conceptualization, Methodology, Investigation, Formal analysis, Writing – original draft, Writing – review & editing. **Guiyao Song:** Methodology, Formal analysis, Writing – review & editing. **Zihao Wang:** Investigation, Validation, Writing – review & editing. **Jianhua Song:** Investigation, Validation, Software. **Qisheng Jiang:** Investigation. **Yangzhou Zhai:** Investigation. **Dianhua Liu:** Supervision, Conceptualization, Methodology, Funding acquisition, Writing – review & editing.

Declaration of Competing Interest

The authors declare that they have no known competing financial interests or personal relationships that could have appeared to influence the work reported in this paper.

Data availability

Data will be made available on request.

Acknowledgments

This work was supported by the National Key R&D Program of China (2017YFB0602204).

Appendix A. Supporting information

Supplementary data associated with this article can be found in the online version at doi:10.1016/j.apcatb.2023.123330.

References

[1] M.S. Yang, S. Liu, J.Q. Sun, M.M. Jin, R. Fu, S.S. Zhang, H.Y. Li, Z.Y. Sun, J. Luo, X. J. Liu, Highly dispersed Bi clusters for efficient rechargeable Zn-CO_2 batteries, Appl. Catal. B Environ. 307 (2022) 8.
[2] W.K. Liu, X.H. Meng, X. Zhao, G. Wang, J.S. Gao, C.M. Xu, Pyrolysis performances of catalytic cracking naphtha and coker naphtha on inert carriers and an active catalyst, Energy Fuels 23 (2009) 5760–5764.
[3] K. Cheng, W. Zhou, J.C. Kang, S. He, S.L. Shi, Q.H. Zhang, Y. Pan, W. Wen, Y. Wang, Bifunctional catalysts for one-step conversion of syngas into aromatics with excellent selectivity and stability, Chem 3 (2017) 334–347.
[4] Z.X. Hua, Y.J. Yang, J. Liu, Direct hydrogenation of carbon dioxide to value-added aromatics, Coord. Chem. Rev. 478 (2023) 38.
[5] J. Wei, R.W. Yao, Q.J. Ge, D.Y. Xu, C.Y. Fang, J.X. Zhang, H.Y. Xu, J. Sun, Precisely regulating Bronsted acid sites to promote the synthesis of light aromatics via CO_2 hydrogenation, Appl. Catal. B Environ. 283 (2021) 11.
[6] T. Wang, C.G. Yang, P. Gao, S.J. Zhou, S.G. Li, H. Wang, Y.H. Sun, $ZnZrO_x$ integrated with chain-like nanocrystal HZSM-5 as efficient catalysts for aromatics synthesis from CO_2 hydrogenation, Appl. Catal. B Environ. 286 (2021) 12.
[7] G.Y. Song, M.Z. Li, L. Xu, X.P. Yang, M.A. Nawaz, H.M. Yuan, Z.X. Zhang, X.M. Xu, D.H. Liu, Tuning the integration proximity between Na promoter and $FeMnO_x$ coupled with rationally modified HZSM-5 to promote selective CO_2 hydrogenation to aromatics, Ind. Eng. Chem. Res. 61 (2022) 6820–6830.
[8] J.M. Liang, L.S. Guo, W.Z. Gao, C.W. Wang, X.Y. Guo, Y.L. He, G.H. Yang, N. Tsubaki, Direct conversion of CO_2 to aromatics over K-Zn-Fe/ZSM-5 catalysts via a Fischer-Tropsch synthesis pathway, Ind. Eng. Chem. Res. 61 (2022) 10336–10346.
[9] H.Y. Yang, Y.R. Dang, X. Cui, X.N. Bu, J. Li, S.G. Li, Y.H. Sun, P. Gao, Selective synthesis of olefins via CO_2 hydrogenation over transition-metal-doped iron-based catalysts, Appl. Catal. B Environ. 321 (2023) 16.
[10] Z.Q. Zhang, G.X. Huang, X.L. Tang, H.R. Yin, J.C. Kang, Q.H. Zhang, Y. Wang, Zn and Na promoted Fe catalysts for sustainable production of high-valued olefins by CO_2 hydrogenation, Fuel 309 (2022) 13.
[11] Y.B. Xu, C.M. Shi, B. Liu, T. Wang, J. Zheng, W.P. Li, D.P. Liu, X.H. Liu, Selective production of aromatics from CO_2, Catal. Sci. Technol. 9 (2019) 593–610.
[12] K. Jin, C.Y. Wen, Q. Jiang, X.Z. Zhuang, L.A. Chen, L.L. Ma, C.G. Wang, Q. Zhang, Conversion of CO_2 to gasoline over tandem Fe/C and HZSM-5 catalysts, Sustain. Energy Fuels 7 (2023) 1265–1272.
[13] C.D. Zhang, G. Kwak, H.G. Park, K.W. Jun, Y.J. Lee, S.C. Kang, S. Kim, Light hydrocarbons to BTEX aromatics over hierarchical HZSM-5: effects of alkali treatment on catalytic performance, Microporous Mesoporous Mater. 276 (2019) 292–301.
[14] C. Zhang, G. Kwak, Y.J. Lee, K.W. Jun, R. Gao, H.G. Park, S. Kim, J.E. Min, S. C. Kang, G.F. Guan, Light hydrocarbons to BTEX aromatics over Zn-modified hierarchical ZSM-5 combined with enhanced catalytic activity and stability, Microporous Mesoporous Mater. 284 (2019) 316–326.
[15] A. Ishihara, Y. Kodama, T. Hashimoto, Aromatics formation by cracking and dehydrocyclization of n-hexane using Zn ion-exchanged ZSM-5-Al_2O_3 hierarchical composite catalysts, React. Kinet. Mech. Catal. 134 (2021) 401–417.
[16] Y. Wang, J. Wu, G. Wang, D.Y. Yang, T. Ishihara, L.M. Guo, Oxygen vacancy engineering in Fe doped akhtenskite-type MnO_2 for low-temperature toluene oxidation, Appl. Catal. B Environ. 285 (2021) 16.
[17] G.Y. Song, M.Z. Li, P.K. Yan, M.A. Nawaz, D.H. Liu, High conversion to aromatics via CO_2-FT over a CO-reduced Cu-Fe_2O_3 catalyst integrated with HZSM-5, ACS Catal. 10 (2020) 11268–11279.

[18] H. Gu, J. Ding, Q. Zhong, Y.Q. Zeng, F.J. Song, Promotion of surface oxygen vacancies on the light olefins synthesis from catalytic CO_2 hydrogenation over Fe-K/ZrO_2 catalysts, Int. J. Hydrog. Energy 44 (2019) 11808–11816.
[19] Y.H. Zheng, C.H. Xu, X. Zhang, Q. Wu, J. Liu, Synergistic effect of alkali Na and K promoter on Fe-Co-Cu-Al catalysts for CO_2 hydrogenation to light hydrocarbons, Catalysts 11 (2021) 11.
[20] H. Jo, M.K. Khan, M. Irshad, M.W. Arshad, S.K. Kim, J. Kim, Unraveling the role of cobalt in the direct conversion of CO_2 to high-yield liquid fuels and lube base oil, Appl. Catal. B Environ. 305 (2022) 15.
[21] B.L. Liang, T. Sun, J.G. Ma, H.M. Duan, L. Li, X.L. Yang, Y.R. Zhang, X. Su, Y. Q. Huang, T. Zhang, Mn decorated Na/Fe catalysts for CO_2 hydrogenation to light olefins, Catal. Sci. Technol. 9 (2019) 456–464.
[22] X.P. Yang, G.Y. Song, M.Z. Li, C.H. Chen, Z.H. Wang, H.M. Yuan, Z.X. Zhang, D. H. Liu, Selective production of aromatics directly from carbon dioxide hydrogenation over nNa-Cu-Fe_2O_3/HZSM-5, Ind. Eng. Chem. Res. 61 (2022) 7787–7798.
[23] Q. Wang, D. Astruc, State of the art and prospects in metal-organic framework (MOF)-based and MOF-derived nanocatalysis, Chem. Rev. 120 (2020) 1438–1511.
[24] W.P. Yang, X.X. Li, Y. Li, R.M. Zhu, H. Pang, Applications of metal-organic-framework-derived carbon materials, Adv. Mater. 31 (2019) 35.
[25] X. Chen, Q. Li, M. Zhang, J.J. Li, S.C. Cai, J. Chen, H.P. Jia, MOF-templated preparation of highly dispersed Co/Al_2O_3 composite as the photothermal catalyst with high solar-to-fuel efficiency for CO_2 methanation, ACS Appl. Mater. Interfaces 12 (2020) 39304–39317.
[26] W.G. Cui, G.Y. Zhang, T.L. Hu, X.H. Bu, Metal-organic framework-based heterogeneous catalysts for the conversion of C1 chemistry: CO, CO_2 and CH_4, Coord. Chem. Rev. 387 (2019) 79–120.
[27] Y. Wang, S. Kazumi, W.Z. Gao, X.H. Gao, H.J. Li, X.Y. Guo, Y. Yoneyama, G. H. Yang, N. Tsubaki, Direct conversion of CO_2 to aromatics with high yield via a modified Fischer-Tropsch synthesis pathway, Appl. Catal. B Environ. 269 (2020) 9.
[28] Y.H. Tong, Y.Z. Wu, Z.L. Xu, L.H. Luo, S.J. Xu, Photocatalytic self-cleaning EVAL membrane by incorporating bio-inspired functionalized MIL-101(Fe) for dye/salt separation, Chem. Eng. J. 444 (2022) 14.
[29] M. Varmazyari, Y. Khani, F. Bahadoran, Z. Shariatinia, S. Soltanali, Hydrogen production employing Cu(BDC) metal-organic framework support in methanol steam reforming process within monolithic micro-reactors, Int. J. Hydrog. Energy 46 (2021) 565–580.
[30] J.T. Tang, J.L. Wang, Iron-copper bimetallic metal-organic frameworks for efficient Fenton-like degradation of sulfamethoxazole under mild conditions, Chemosphere 241 (2020) 9.
[31] W.X. Li, J. Cao, W.P. Xiong, Z.H. Yang, S.W. Sun, M.Y. Jia, Z.Y. Xu, In-situ growing of metal-organic frameworks on three-dimensional iron network as an efficient adsorbent for antibiotics removal, Chem. Eng. J. 392 (2020) 9.
[32] A. Hamedi, F. Trotta, M. Borhani Zarandi, M. Zanetti, F. Caldera, A. Anceschi, M. R. Nateghi, In situ synthesis of MIL-100(Fe) at the surface of Fe_3O_4@AC as highly efficient dye adsorbing nanocomposite, Int. J. Mol. Sci. 20 (2019) 20.
[33] C. Sarkar, J.K. Basu, A.N. Samanta, Synthesis of MIL-53(Fe)/SiO_2 composite from LD slag as a novel photo-catalyst for methylene blue degradation, Chem. Eng. J. 377 (2019) 9.
[34] G.I. Dzhardimalieva, R.K. Baimuratova, E.I. Knerelman, G.I. Davydova, S. E. Kudaibergenov, O.V. Kharissova, V.A. Zhinzhilo, I.E. Uflyand, Synthesis of copper(II) trimesinate coordination polymer and its use as a sorbent for organic dyes and a precursor for nanostructured material, Polymers 12 (2020) 22.
[35] C.X. Lu, Y.Z. Zhou, L.Z. Li, H.W. Chen, L.S. Yan, Conversion of glucose into 5-hydroxymethylfurfural catalyzed by Cr-and Fe-containing mixed-metal metal-organic frameworks, Fuel 333 (2023) 8.
[36] L. He, Y.N. Dong, Y.N. Zheng, Q.M. Jia, S.Y. Shan, Y.Q. Zhang, A novel magnetic MIL-101(Fe)/TiO_2 composite for photo degradation of tetracycline under solar light, J. Hazard. Mater. 361 (2019) 85–94.
[37] J. Yang, Y.J. Ren, J.S. Lu, H.P. Liu, Z.Q. Zhang, H.L. Pang, K. Bounkhong, Chemical looping gasification with a $CuFe_2O_4$-enhanced phosphogypsum oxygen carrier during reduction in a fluidized bed reactor, Chem. Eng. J. 426 (2021) 14.
[38] K. Gu, E.J. Kim, S.K. Sharma, P.R. Sharma, S. Bliznakov, B.S. Hsiao, M. H. Rafailovich, Mesoporous carbon aerogel with tunable porosity as the catalyst support for enhanced proton-exchange membrane fuel cell performance, Mater. Today Energy 19 (2021) 9.
[39] J.M. Cho, S.R. Lee, J. Sun, N. Tsubaki, E.J. Jang, J.W. Bae, Highly ordered mesoporous Fe_2O_3-ZrO_2 bimetal oxides for an enhanced CO hydrogenation activity to hydrocarbons with their structural stability, ACS Catal. 7 (2017) 5955–5964.
[40] H.F. Tian, J.P. Jiao, F. Zha, X.J. Guo, X.H. Tang, Y. Chang, H.S. Chen, Hydrogenation of CO_2 into aromatics over ZnZrO-Zn/HZSM-5 composite catalysts derived from ZIF-8, Catal. Sci. Technol. 12 (2022) 799–811.
[41] M. Amoyal, R. Vidruk-Nehemya, M.V. Landau, M. Herskowitz, Effect of potassium on the active phases of Fe catalysts for carbon dioxide conversion to liquid fuels through hydrogenation, J. Catal. 348 (2017) 29–39.
[42] L.Z. Jiang, K.L. Liu, S.F. Hung, L.Y. Zhou, R.X. Qin, Q.H. Zhang, P.X. Liu, L. Gu, H. M. Chen, G. Fu, N.F. Zheng, Facet engineering accelerates spillover hydrogenation on highly diluted metal nanocatalysts, Nat. Nanotechnol. 15 (2020) 848.
[43] R.F. Wang, B.L. Liang, X.L. Yang, X.N. Li, Y.R. Zhang, G.D. Liu, X. Su, Y.Q. Huang, T. Zhang, Critical role of sodium migration in iron-based FT- zeolite tandem catalyst system for syngas hydrogenation to gasoline, Appl. Catal. B Environ. 322 (2023) 10.
[44] K.O. Otun, Y.L. Yao, X.Y. Liu, D. Hildebrandt, Synthesis, structure, and performance of carbide phases in Fischer-Tropsch synthesis: a critical review, Fuel 296 (2021) 22.
[45] S. Jo, J.H. Lee, T.Y. Kim, J.H. Woo, H.J. Ryu, B. Hwang, S.C. Lee, J.C. Kim, K. L. Gilliard-Abdulaziz, A fundamental study of CO_2 capture and CH_4 production in a rapid cyclic system using nickel-lithium-silicate as a catal-sorbent, Fuel 311 (2022) 9.
[46] M.Z. Li, M.A. Nawaz, G.Y. Song, W.Q. Zaman, D.H. Liu, Influential role of elemental migration in a composite iron-zeolite catalyst for the synthesis of aromatics from syngas, Ind. Eng. Chem. Res. 59 (2020) 9043–9054.
[47] B. Liu, S.S. Geng, J. Zheng, X.L. Jia, F. Jiang, X.H. Liu, Unravelling the new roles of Na and Mn promoter in CO_2 hydrogenation over Fe_3O_4-based catalysts for enhanced selectivity to light-olefins, ChemCatChem 10 (2018) 4718–4732.
[48] P.A. Chernavskii, V.O. Kazak, G.V. Pankina, Y.D. Perfiliev, T. Li, M. Virginie, A. Y. Khodakov, Influence of copper and potassium on the structure and carbidisation of supported iron catalysts for Fischer-Tropsch synthesis, Catal. Sci. Technol. 7 (2017) 2325–2334.
[49] Y.M. Liu, D.S. Mao, J. Yu, Y.L. Zheng, X.M. Guo, Facile preparation of highly active and stable CuO-CeO_2 catalysts for low-temperature CO oxidation via a direct solvothermal method, Catal. Sci. Technol. 10 (2020) 8383–8395.
[50] Y. Han, C.Y. Fang, X.W. Ji, J. Wei, Q.J. Ge, J. Sun, Interfacing with carbonaceous potassium promoters boosts catalytic CO_2 hydrogenation of iron, ACS Catal. 10 (2020) 12098–12108.
[51] N. Utsis, M.V. Landau, A. Erenburg, R.V. Nehemya, M. Herskowitz, Performance of reverse water gas shift on coprecipitated and C-templated BaFe-hexaaluminate: the effect of Fe loading, texture, and promotion with K, ChemCatChem 10 (2018) 3795–3805.
[52] P. Hongmanorom, J. Ashok, P. Chirawatkul, S. Kawi, Interfacial synergistic catalysis over Ni nanoparticles encapsulated in mesoporous ceria for CO_2 methanation, Appl. Catal. B Environ. 297 (2021) 13.
[53] K. Kahler, M.C. Holz, M. Rohe, J. Strunk, M. Muhler, Probing the reactivity of ZnO and Au/ZnO nanoparticles by methanol adsorption: a TPD and DRIFTS study, ChemPhysChem 11 (2010) 2521–2529.
[54] M.K. Khan, P. Butolia, H. Jo, M. Irshad, D. Han, K.W. Nam, J. Kim, Selective conversion of carbon dioxide into liquid hydrocarbons and long-chain alpha-olefins over Fe-amorphous AlO_x bifunctional catalysts, ACS Catal. 10 (2020) 10325–10338.
[55] Z.M. Wang, M.Q. Xiao, X.X. Wang, H. Wang, X. Chen, W.X. Dai, Y. Yu, X.Z. Fu, Thermo-driven photocatalytic CO_2 hydrogenation over NiO_x/Nb_2O_5 via regulating the electron transfer behavior of reactant gas adsorption, Appl. Surf. Sci. 592 (2022) 12.
[56] W.J. He, Y.C. Wei, J. Xiong, Z.L. Tang, Y.L. Wang, X. Wang, J.G. Deng, X.L. Yu, X. Zhang, Z. Zhao, Boosting selective photocatalytic $CO_{(2)}$ reduction to CO over dual-core@shell structured Bi_2O_3/Bi_2WO_6@g-C_3N_4 catalysts with strong interaction interface, Sep. Purif. Technol. 300 (2022) 13.
[57] S. Das, J. Perez-Ramirez, J.L. Gong, N. Dewangan, K. Hidajat, B.C. Gates, S. Kawi, Core-shell structured catalysts for thermocatalytic, photocatalytic, and electrocatalytic conversion of CO_2, Chem. Soc. Rev. 49 (2020) 2937–3004.
[58] C.C. Jin, Y. Zhou, S.B. Han, W.J. Shen, Water-assisted low-temperature oxidation of CO at the Au-Fe_2O_3 interface, J. Phys. Chem. C 125 (2021) 26031–26038.
[59] M.J. Xu, X.L. Liu, G.Y. Song, Y.Y. Cai, B.F. Shi, Y.T. Liu, X.X. Ding, Z.X. Yang, P. F. Tian, C.X. Cao, J. Xu, Regulating iron species compositions by Fe-Al interaction in CO_2 hydrogenation, J. Catal. 413 (2022) 331–341.
[60] D. Xu, M.Y. Ding, X.L. Hong, G.L. Liu, S.C.E. Tsang, Selective $C_{-2(+)}$ alcohol synthesis from direct CO_2 hydrogenation over a Cs-promoted Cu-Fe-Zn catalyst, ACS Catal. 10 (2020) 5250–5260.
[61] S.X. Bai, Q. Shao, P.T. Wang, Q.G. Dai, X.Y. Wang, X.Q. Huang, Highly active and selective hydrogenation of CO_2 to ethanol by ordered Pd-Cu nanoparticles, J. Am. Chem. Soc. 139 (2017) 6827–6830.
[62] S. Kattel, B.H. Yan, Y.X. Yang, J.G.G. Chen, P. Liu, Optimizing binding energies of key intermediates for CO_2 hydrogenation to methanol over oxide-supported copper, J. Am. Chem. Soc. 138 (2016) 12440–12450.
[63] X.W. Nie, H.Z. Wang, M.J. Janik, Y.G. Chen, X.W. Guo, C.S. Song, Mechanistic insight into C-C coupling over Fe-Cu bimetallic catalysts in CO_2 hydrogenation, J. Phys. Chem. C 121 (2017) 13164–13174.
[64] X.W. Nie, H.Z. Wang, M.J. Janik, X.W. Guo, C.S. Song, Computational investigation of Fe-Cu bimetallic catalysts for CO_2 hydrogenation, J. Phys. Chem. C 120 (2016) 9364–9373.
[65] Z.M. Wang, X.X. Wang, H. Wang, X. Chen, W.X. Dai, X.Z. Fu, The role of electron transfer behavior induced by CO chemisorption on visible-light-driven CO conversion over WO_3 and $CuWO_4$/WO_3, Appl. Catal. B Environ. 265 (2020) 15.
[66] T.K. Liu, Y.Y. Yao, L.Q. Wei, Z.F. Shi, L.Y. Han, H.X. Yuan, B. Li, L.H. Dong, F. Wang, C.Z. Sun, Preparation and evaluation of copper manganese oxide as a high-efficiency catalyst for CO oxidation and NO reduction by CO, J. Phys. Chem. C 121 (2017) 12757–12770.
[67] D. Xu, M.Y. Ding, X.L. Hong, G.L. Liu, Mechanistic aspects of the role of K promotion on Cu-Fe-based catalysts for higher alcohol synthesis from CO_2 hydrogenation, ACS Catal. 10 (2020) 14516–14526.
[68] F. Yuan, G.H. Zhang, M.R. Wang, J. Zhu, M. Zhang, F.S. Ding, Z.N. Cheng, C. S. Song, X.W. Guo, Boosting the production of light olefins from CO_2 hydrogenation over Fe-Co bimetallic catalysts derived from layered double hydroxide, Ind. Eng. Chem. Res. 62 (2023) 8210–8221.
[69] T. Herranz, S. Rojas, F.J. Perez-Alonso, M. Ojeda, P. Terreros, J.L.G. Fierro, Genesis of iron carbides and their role in the synthesis of hydrocarbons from synthesis gas, J. Catal. 243 (2006) 199–211.
[70] K.H. Han, S. Wang, N. Hu, W.D. Shi, F.G. Wang, Alloying Ni-Cu nanoparticles encapsulated in SiO_2 nanospheres for synergistic catalysts in CO_2 reforming with methane reaction, ACS Appl. Mater. Interfaces 14 (2022) 23487–23495.